Comparison of Eulerian Bin and Lagrangian Particle-Based Microphysics in Simulations of Nonprecipitating Cumulus

WOJCIECH W. GRABOWSKI[a]

[a] *Mesoscale and Microscale Meteorology Laboratory, National Center for Atmospheric Research, Boulder, Colorado*

(Manuscript received 2 April 2020, in final form 28 August 2020)

ABSTRACT: A single nonprecipitating cumulus congestus setup is applied to compare droplet spectra grown by the diffusion of water vapor in Eulerian bin and particle-based Lagrangian microphysics schemes. Bin microphysics represent droplet spectral evolution applying the spectral density function. In the Lagrangian microphysics, computational particles referred to as superdroplets are followed in time and space with each superdroplet representing a multiplicity of natural cloud droplets. The same cloud condensation nuclei (CCN) activation and identical representation of the droplet diffusional growth allow the comparison. The piggybacking method is used with the two schemes operating in a single simulation, one scheme driving the dynamics and the other one piggybacking the simulated flow. Piggybacking allows point-by-point comparison of droplet spectra predicted by the two schemes. The results show the impact of inherent limitations of the two microphysics simulation methods, numerical diffusion in the Eulerian scheme and a limited number of superdroplets in the Lagrangian scheme. Numerical diffusion in the Eulerian scheme results in a more dilution of the cloud upper half and thus smaller cloud droplet mean radius. The Lagrangian scheme typically has larger spatial fluctuations of droplet spectral properties. A significantly larger mean spectral width in the bin microphysics across the entire cloud depth is the largest difference between the two schemes. A fourfold increase of the number of superdroplets per grid volume and a twofold increase of the spectral resolution and thus the number of bins have small impact on the results and provide only minor changes to the comparison between simulated cloud properties.

KEYWORDS: Cloud droplets; Cloud microphysics; Cumulus clouds

1. Introduction

Understanding processes affecting cloud droplet spectra is an important objective of observational and modeling cloud studies. Droplet spectral characteristics impact such essential processes as the precipitation development or radiative transfer through a cloudy atmosphere. In cloud modeling, simulation of droplet spectral evolution is cumbersome and often simpler approaches such as the bulk microphysics are used. For predicting the spectra, there are essentially two different possibilities. The first one, the so-called bin (or spectral) microphysics, solves the evolution equation for the spectral density function with the droplet spectrum represented by a finite number of droplet radius (or mass) bins. Each bin is advected in the physical space, and all bins are combined in each model grid box to represent droplet growth through the transport (advection) of droplets from one bin to another. This is the Eulerian approach because the spectral density function is formulated and solved similarly to other Eulerian fluid flow variables such as the fluid velocity, air temperature, and water vapor mixing ratio. Bin microphysics is the traditional approach to model spectral evolution of cloud and precipitation particles (see Khain et al. 2015; Grabowski et al. 2019 and references therein). The second approach is to represent evolution of the droplet spectrum by an ensemble of Lagrangian point particles. These particles are tracked in the physical space using model-predicted flow field, and they grow or evaporate as they move with the flow. Each computational particle represents a multitude of natural cloud particles and an additional parameter, the multiplicity, is used to describe the total number of real particles each computational particle represents. For warm-rain microphysics, the computational particles are often called superdroplets and the approach is referred to as the superdroplet method (Shima et al. 2009). Superdroplet method is a relatively novel approach to simulate droplet spectral evolution; see Andrejczuk et al. (2008, 2010), Shima et al. (2009), Sölch and Kärcher (2010), Riechelmann et al. (2012), Hoffmann et al. (2015), and Grabowski et al. (2019).

The two schemes represent drastically different simulation methodologies and their direct comparison is needed. To that end, Grabowski (2020; G20 hereafter) presents such a comparison applying a cloud chamber setup. The chamber, a laboratory apparatus at the Michigan Technological University (see http://phy.sites.mtu.edu/cloudchamber/), forms a cloud because of the temperature and humidity differences between lower and upper horizontal boundaries that drive turbulent Rayleigh–Bénard convection. Mixing between plumes rising and descending from the lower and upper boundary, respectively, results in the cloud condensation nuclei (CCN) activation and cloud droplet growth. Motivated by simulations discussed in Thomas et al. (2019), G20 considers only CCN activation and droplet growth by the diffusion of water vapor. G20 shows a good agreement between droplet spectra predicted by the two modeling methodologies when averaged over the chamber volume away from boundaries. Small differences that do exist are explained by the inherent differences between

Corresponding author: Wojciech Grabowski, grabow@ucar.edu

Publisher's Note: This article was revised on 25 January 2021 to correct the title of the Grabowski (2019) reference.

DOI: 10.1175/JAS-D-20-0100.1

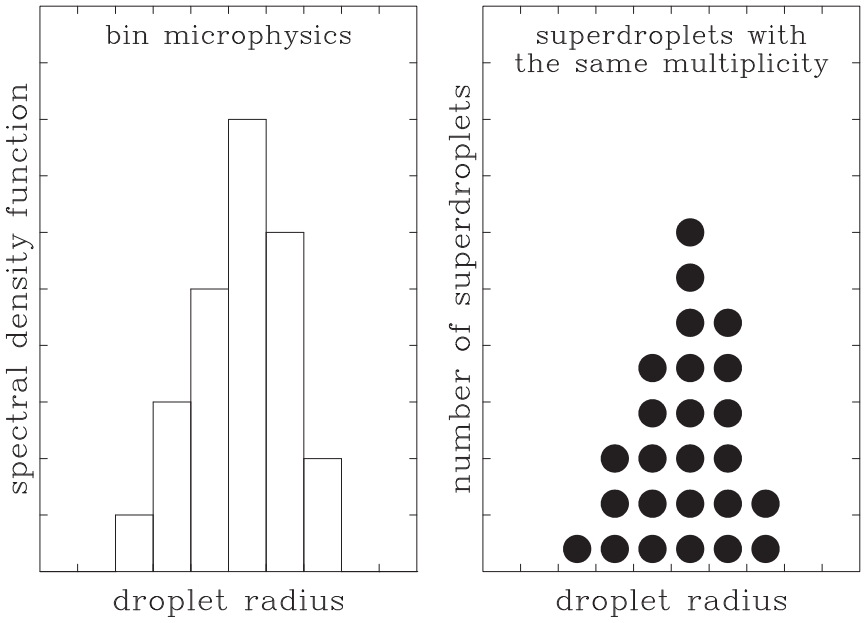

FIG. 1. Schematic of the droplet size distribution in (left) Eulerian bin microphysics and (right) Lagrangian superdroplet scheme.

the two schemes and their numerical implementation. There are large differences in the local droplet spectra, again in agreement with the limitations of the theoretical foundation behind the two approaches. There is a general agreement between the simulations and cloud chamber observations, with simplifications of the CCN activation and of the droplet growth equation used in the simulations likely explaining specific differences.

In this paper, we consider the problem of predicting cloud droplet spectra in a natural cloud, a nonprecipitating cumulus congestus. In general, droplet spectra observed in natural cumuli, even in undiluted or weakly diluted volumes, are often significantly wider than predicted by simple models of cloud dynamics and microphysics; see, for instance, Fig. 11 in Jensen et al. (1985) or Fig. 1 in Lasher-Trapp et al. (2005, LT05 hereafter) and their discussion; Brenguier and Chaumat (2001); among many others. This problem continues to occupy cloud physics community from early days of in situ aircraft observations of cloud microphysics (e.g., Warner 1969). On the modeling side, bin microphysics is affected by numerical issues similar to other Eulerian fields. For instance, typically sharp cloud–environment boundary can only be represented by relatively smooth few-gridpoint transition zones. Because each bin is advected separately, one may expect unphysical droplet spectra within those zones. Since high-quality contemporary advection schemes are nonlinear, separate bin advection typically results in numerical artifacts (Ovtchinnikov and Easter 2009). Moreover, as documented in Morrison et al. (2018), combination of the bin advection in the stratified atmosphere with advection in the bin space that represents droplet growth typically results in numerical problems such as artificial spectral broadening. The Lagrangian particle-based microphysics is free from these issues, but suffers from the limited and usually small number of superdroplets, especially considering the number of real droplets in a simulated cloud.

The above differences between the two approaches to droplet spectral modeling warrant comparison in simulations of a cumulus cloud. As noted in G20, decoupling between the vertical transport and condensational growth of cloud droplets (because of the constant chamber pressure) likely plays role in good G20 comparison. In a warm cumulus simulation, the coupling between vertical advection and condensational growth/evaporation may lead to a different conclusion (Morrison et al. 2018). However, replacing one microphysics scheme with another in a cumulus simulation typically leads to a different cloud evolution, and this make comparison between the two simulations difficult. To cope with this problem, we apply the piggybacking methodology (see Grabowski 2019, and references therein). The next section presents the dynamic model, the setup of cumulus congestus simulations, and explains the piggybacking method. Section 3 presents simulation results focusing on the comparison between droplet spectra predicted by the two schemes. Sensitivity simulations with an increased number of superdroplets in the Lagrangian scheme and an increased spectral resolution in the bin scheme are discussed in section 4. Discussion in section 5 concludes the paper.

2. The model, methodology, and model setup

a. Dynamics

The dynamic model, the same as in G20, is a simplified serial version of the 3D finite-difference nonhydrostatic anelastic Eulerian–Lagrangian (EULAG) model (http://www.mmm.ucar.edu/eulag/) referred to as babyEULAG. BabyEULAG features Eulerian dynamics and has been

previously applied in simulations of shallow and deep convection (e.g., Grabowski 2014, 2015; Grabowski and Jarecka 2015; Grabowski and Morrison 2016, 2017). Here, we apply babyEULAG to simulate a single ice-free nonprecipitating cumulus congestus cloud following LT05. The model has no subgrid-scale (SGS) transport scheme and relies on the monotone MPDATA advection scheme (Smolarkiewicz 1984; Smolarkiewicz and Clark 1986; Smolarkiewicz and Grabowski 1990) to provide small-scale dissipation. This is in the spirit of the so-called implicit large-eddy simulation (ILES; Margolin and Rider 2002; Andrejczuk et al. 2004; Margolin et al. 2006; Grinstein et al. 2007). ILES removes the need of selecting a suitable SGS scheme not only for the dynamics, but for thermodynamic variables as well. There are significant differences in SGS methodologies that can be used for the two microphysical schemes. For the bin scheme, the traditional approach is based on the concept of Reynolds averaging and ensemble-averaged SGS fluxes. For the Lagrangian scheme, the approach can be based on a stochastic realization of the SGS processes that affect the motion and growth of Lagrangian particle (e.g., Weil et al. 2004; Sölch and Kärcher 2010; Grabowski and Abade 2017; Abade et al. 2018; Hoffmann et al. 2019).[1] If SGS schemes are used, the results will be affected by those differences as well. Before exploring those, however, it is appropriate to understand the differences in simulations affected by numerical aspects alone.

To simulate a single cumulus cloud, we follow methodology applied in LT05. Horizontally uniform surface temperature and moisture fluxes are applied during the first simulation hour and they lead to the development of the boundary layer turbulent eddies. The surface fluxes have amplitudes of $0.1\,\mathrm{K\,m\,s^{-1}}$ and $4\times10^{-5}\,\mathrm{m\,s^{-1}}$ for the temperature and water vapor mixing ratio, respectively. In the second hour, a single cloud in the center of the domain is forced by Gaussian-shaped surface fluxes. The fluxes have 1.7-km half width and the maximum values at the center of the domain 3 times larger than the uniform fluxes during the first hour. Surface momentum fluxes are prescribed assuming a constant friction velocity of $0.28\,\mathrm{m\,s^{-1}}$ as in Siebesma et al. (2003). Temperature, water vapor, and momentum tendencies due to surface fluxes are derived assuming the fluxes exponentially decrease with height with the *e*-folding length of 200 m. A random noise of 10% amplitude is added to the surface fluxes to break the uniform conditions at the simulation onset and provide small-scale perturbations during the model run. The initial sounding provided by Prof. Lasher-Trapp comes from observation during the Small Cumulus Microphysics Study (SCMS); see LT05. The computational domain of $8^3\,\mathrm{km}^3$ that is covered with a uniform 128^3 grid with the grid length of 62.5 m. The domain is periodic in the horizontal with rigid lid free-slip boundary conditions at the surface and top. The dynamic model time step is 1 s with 0.25-s substepping for the two microphysics schemes (see details in Grabowski and Jarecka 2015).

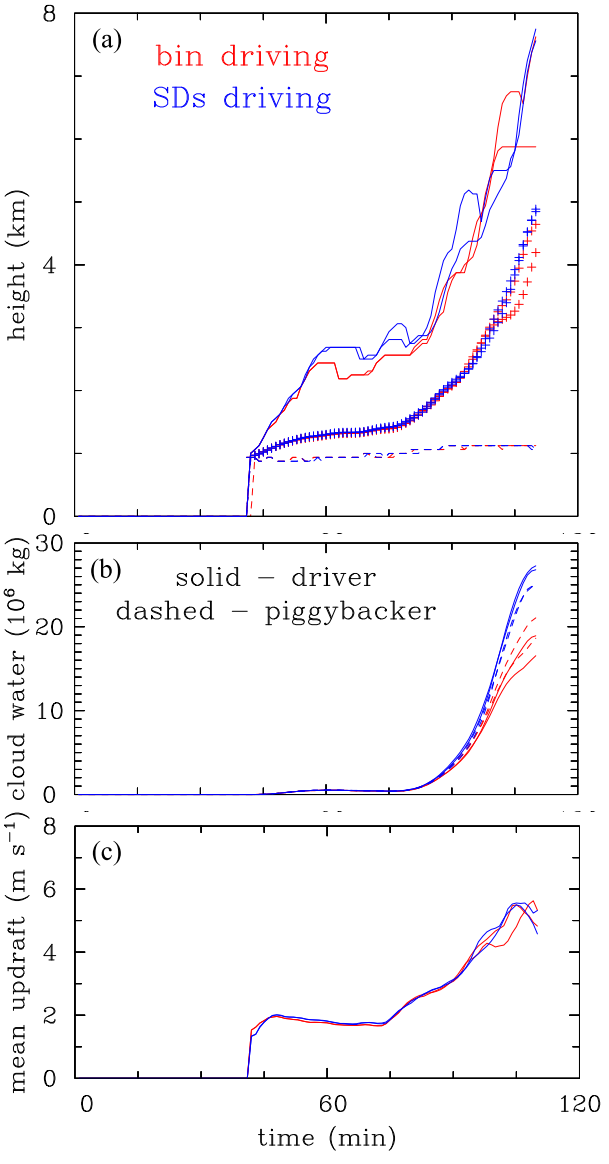

FIG. 2. Results from four piggybacking simulations. Evolutions of (a) the cloud-base height (dashed lines), cloud-top height (solid lines), and cloud water center-of-mass height (plus symbols) in four drivers; (b) the total cloud water in the domain in drivers (solid lines) and piggybackers (dashed lines); and (c) the mean vertical velocity in grid volumes with driver cloud water mixing ratio larger than $0.1\,\mathrm{g\,kg^{-1}}$ and vertical velocity larger than $1\,\mathrm{m\,s^{-1}}$. Results are shown up to minute 110 only.

A unique feature of the current study is the piggybacking methodology. Because moist convection is a chaotic system, changing the microphysics scheme (or even a scheme parameter) typically leads to a different cloud evolution. In such a case, a comparison between simulations is only possible through statistical methods, for instance, comparing droplet distributions at a selected height and featuring the same

[1] These differences are similar to the representation of droplet collision–coalescence applying the Smoluchowski equation in the Eulerian scheme and using the probabilistic collision–coalescence algorithm in the Lagrangian scheme; see discussion in Grabowski et al. (2019).

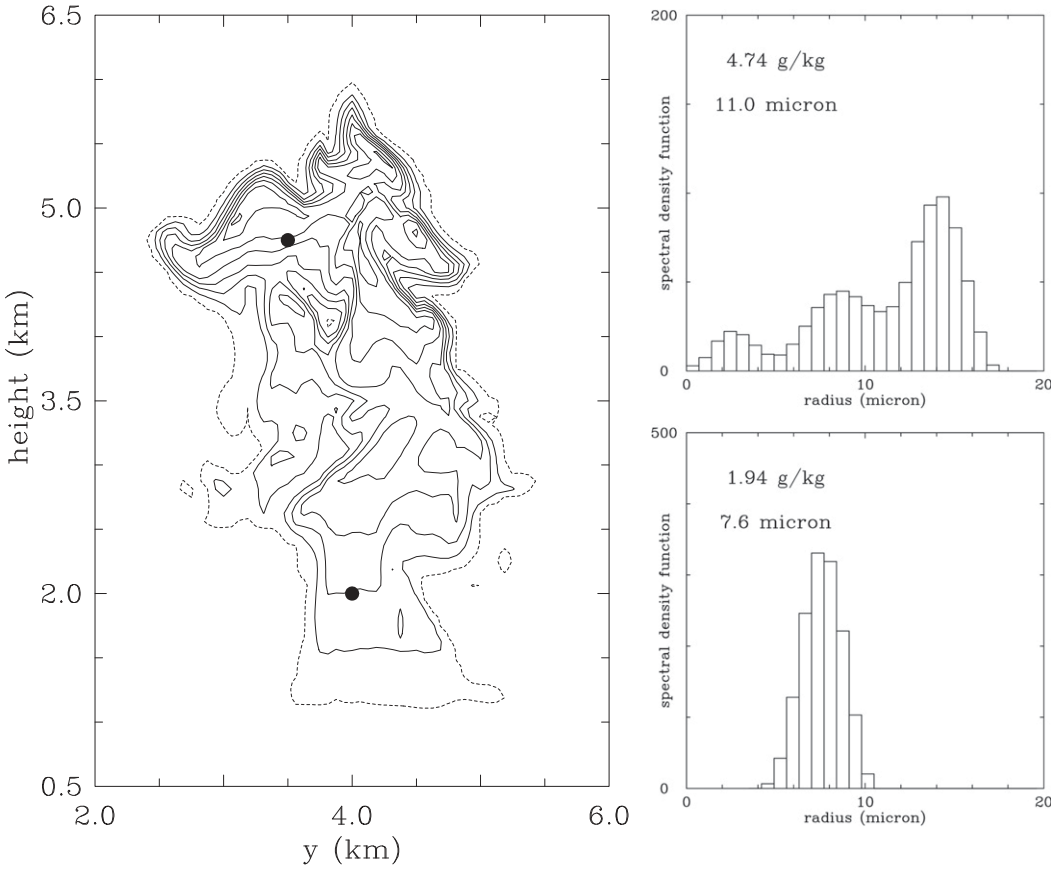

FIG. 3. Example of bin microphysics results for minute 106 from one of piggybacking simulations. (left) Contours of the cloud water mixing ratio in the central x plane of the 3D cloud. Only part of the entire computational domain is shown. Dashed contour is for 0.1 g kg^{-1}. Solid contour interval is 1 g kg^{-1}. The two dots show locations at which droplet spectra are shown. (right) Droplet spectra (see dots in the left panel), along with the total cloud water mixing ratio and the mean radius.

adiabatic liquid water fraction. The key idea behind piggybacking is to apply two sets of thermodynamic variables (the temperature, water vapor, and all aerosol, cloud, and precipitation variables) in a single simulation. One thermodynamic set is used in the buoyancy calculation and thus it is coupled to the dynamics. That set drives the simulated flow and it is referred to as the driver. The second thermodynamic set piggybacks the flow, that is, thermodynamic variables are carried by the flow but they do not affect it. The set is referred to as the piggybacker. Piggybacking allows comparing microphysical details independent of different flow realizations because the two schemes operate in the same cloud-scale flow. See a recent review of the piggybacking method featuring a list of its applications in Grabowski (2019). Here, we apply piggybacking to contrast the Eulerian bin microphysics scheme and the particle-based Lagrangian scheme in simulations of a nonprecipitating warm cumulus. The two schemes are briefly discussed below.

b. *Microphysics*

The Eulerian bin microphysics scheme is the same as applied in shallow nonprecipitating convection simulations discussed in Grabowski and Jarecka (2015). The scheme considers 30 equally spaced bins with the radius bin size of 0.7 μm spanning the radius range from 0 to 21 μm. Activated droplets are inserted in the first bin. Each bin is independently advected in the physical space using the same MPDATA scheme as applied to the momentum, temperature, and water vapor mixing ratio. Droplet sedimentation is not considered. All bins are combined at each grid box to calculate evolution of the droplet spectrum due to the local sub- or supersaturation applying a custom-designed 1D advection scheme. The scheme combines the analytic Lagrangian solution of the condensational growth with remapping of the spectral distribution onto the original radius grid using piecewise linear functions (see section 3.2 in Grabowski et al. 2011).

The particle-based Lagrangian scheme follows Grabowski et al. (2018). The specific implementation considers on average 30 Lagrangian particles (superdroplets) per cloudy grid box, each featuring the same multiplicity (see the CCN activation below). Although arguably quite small, simulations presented in G20 document that the number as small as 10 per grid box provides physically meaningful results. Each activated superdroplet is placed at a random position within

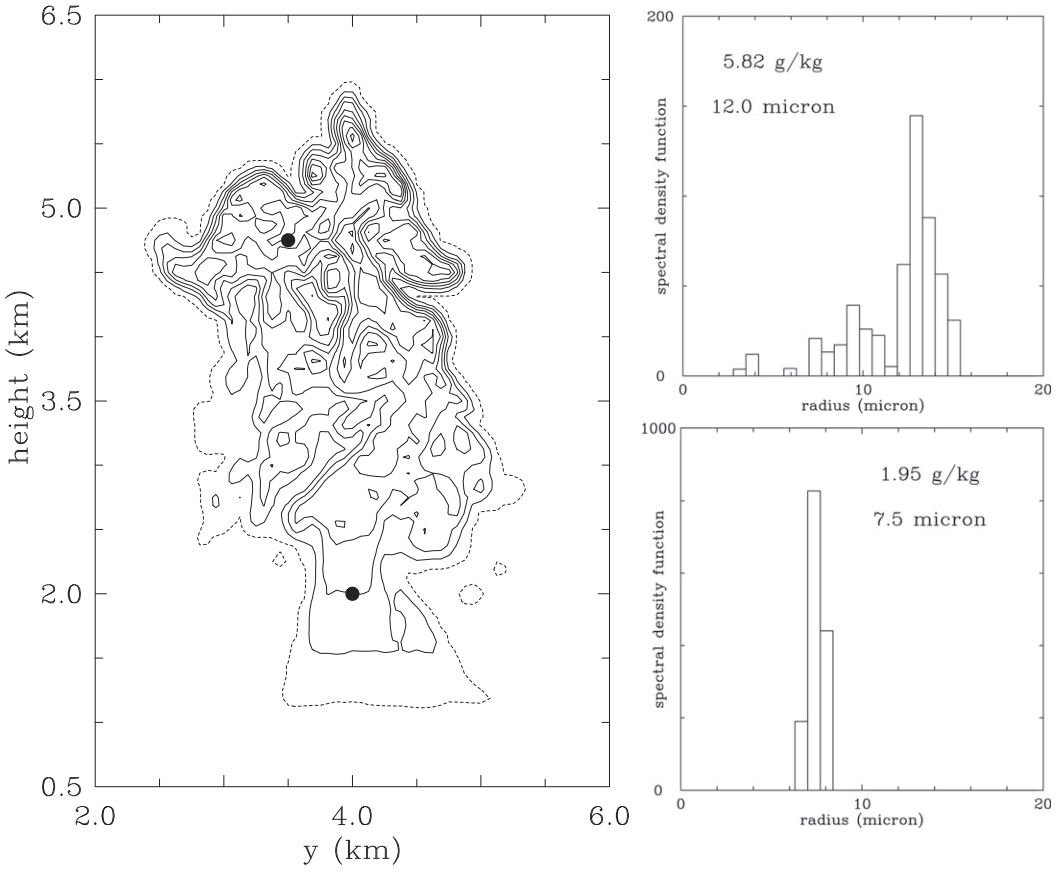

FIG. 4. As in Fig. 3, but for the superdroplet microphysics. The original data are averaged as explained in text.

the grid box. Superdroplets are advected applying a model flow field interpolated to the droplet position as in Arabas et al. (2015). The interpolation scheme maintains the incompressibility of the flow at subgrid scales; see discussion of this aspect in section 2.4 in Grabowski et al. (2018). As in the bin scheme, droplet sedimentation is not considered. The activated CCN is assumed to have a radius of 0.7 μm with a 0.2-μm random component to mimic the finite bin width of the Eulerian scheme.

We apply Twomey CCN activation to represent the initial formation of cloud droplets in the two schemes. The Twomey activation relates the concentration N of activated CCN to the local supersaturation S (in percent) as $N = C_0 S^k$, where C_0 and k are coefficients based on the observed characteristics of the CCN (Twomey 1959; see also Pruppacher and Klett 1997). Based on SCMS observations, LT05 suggests using $C_0 = 1114\,\mathrm{cm}^{-3}$ and $k = 0.77$. In addition, we limit N to a maximum value of $N_{\max} = 1150\,\mathrm{cm}^{-3}$. In the numerical implementation, the concentration of cloud droplets within each grid box is calculated first in both schemes. If the concentration is smaller than the concentration of activated CCN N resulting from the Twomey formula applying the local supersaturation, additional droplets need to be added to the grid box up to N. This is straightforward for the bin scheme, but requires additional considerations for the Lagrangian scheme because of the finite number of equal-multiplicity superdroplets, 30 in the current simulations. The new superdroplets are created in installments of $N_{\max}/30$ ensuring the maximum number of superdroplets within the grid box does not exceed 30. This is the Twomey activation as described in Grabowski et al. (2018, see section 2.3 and Fig. 1 therein). The vertical grid length used in the simulations is too coarse to accurately predict the concentration of cloud droplets activated at the cloud base (Clark 1974; Morrison and Grabowski 2008; Grabowski and Jarecka 2015). This is arguably of secondary importance as long as the two schemes apply only resolved cloud-base supersaturation and do not include an SGS scheme that can affect the cloud-base activation in different ways between the two schemes.

Droplet growth in both schemes is calculated applying a simplified growth formula:

$$dr/dt = AS/(r + r_0),$$

with $A = 0.9152 \times 10^{-10}\,\mathrm{m}^2\,\mathrm{s}^{-1}$ and $r_0 = 1.86\,\mu$m; see appendix in Grabowski and Jarecka [2015; Eq. (A6) in particular] and Eq. (4) in Grabowski et al. (2018). Incorporation of r_0 in the droplet growth equation allows including kinetic effects in a simplified way and limits the rate when r approaches zero. For a fair comparison, the two schemes have to apply the same droplet growth equation and this is why the solution effect is neglected as impossible to include in the bin scheme;

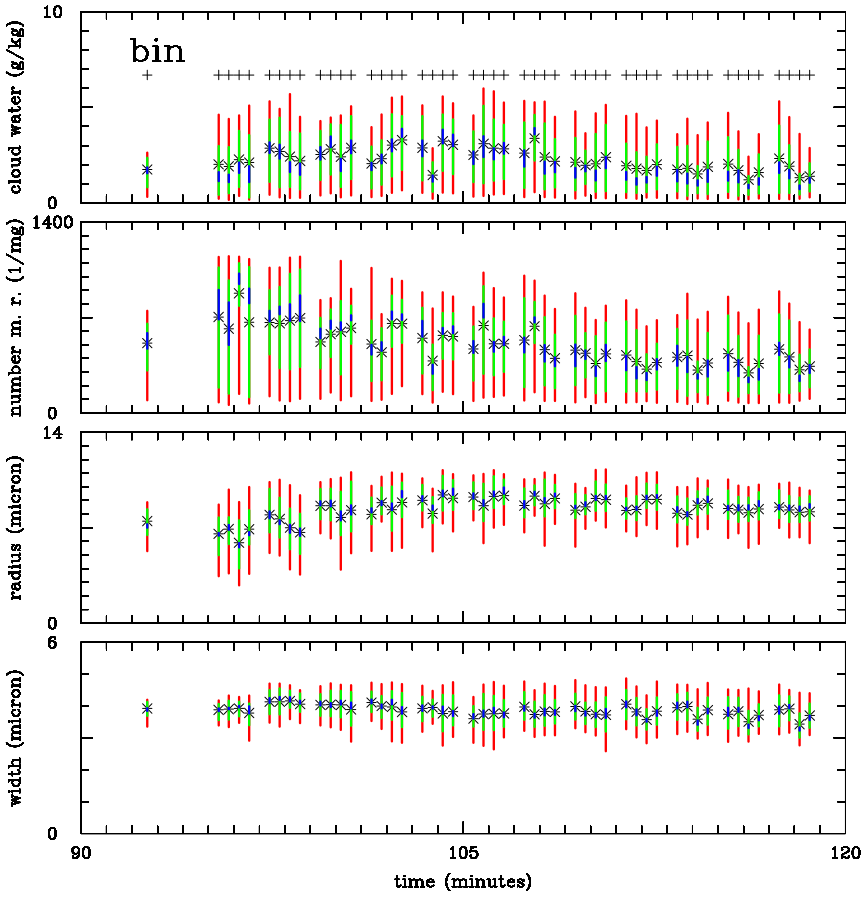

FIG. 5. Evolutions of the bin simulation results at 4-km height. (top) The mean liquid water mixing ratio, (second) mean droplet number mixing ratio (m. r.), (third) mean droplet radius, and (bottom) mean spectral width. Only cloudy points with the cloud water mixing ratio larger than 0.1 g kg^{-1} are included. Thick lines show cloud percentile ranges: red is for 10th–90th, green is for 25th–75th, and blue is for 45th–55th. Stars show the mean values. Plus symbols in the top panel show the adiabatic cloud water mixing ratio. The figure includes data from two driving and two piggybacking sets. Results are shown every 2 min with individual sets shown shifted from the actual minute for clarity.

see discussion in Kogan (1991). The curvature effect is only important for small droplets and is neglected as well. The two schemes apply the droplet growth equation in different ways: as a transport (advection) velocity across the bin space in the Eulerian scheme and to calculate individual superdroplet growth in the Lagrangian scheme.

Figure 1 illustrates the representation of the droplet size distribution in both schemes. In the bin scheme, the distribution is simulated directly by solving the evolution equation for the spectral density function, e.g., (4) in Grabowski et al. (2011) or (A6) in Grabowski and Jarecka (2015). In the particle-based Lagrangian scheme, superdroplets within each grid box can be gathered into size bins that correspond to the Eulerian bins as illustrated in the right panel.

c. *Model simulations*

Two simulation sets were completed. The first set features four piggybacking simulations, two with superdroplets driving and bin piggybacking, and two with bin driving and superdroplets piggybacking. The piggybacking simulations allow comparison of cloud characteristics in each grid volume because the two schemes operate in exactly the same cloud-scale flow. The reason for two simulations with each scheme driving is to assess with a better confidence if there are any systematic differences depending on which scheme drives the simulation. Results of piggybacking simulations are discussed in the next section. The second set of six traditional simulations (i.e., no piggybacking), each with a single set of thermodynamics variables, three with bin microphysics and three with superdroplets, applies the same spatial resolution as the first set, but an increased bin resolution in the Eulerian scheme and increased number of superdroplets in the Lagrangian scheme. Unfortunately, the sensitivity simulations cannot be run in the piggybacking mode because of the increased computational cost. Results of these simulations are discussed in section 4. In the two sets, different cloud evolutions come

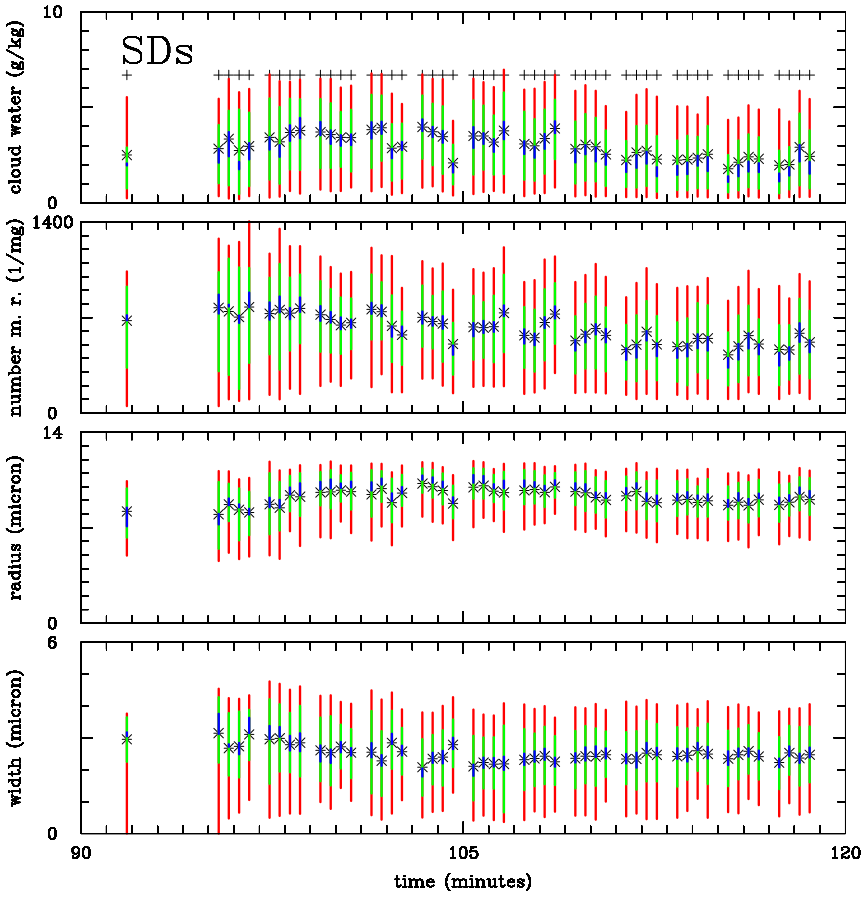

FIG. 6. As in Fig. 5, but for the simulation with superdroplets.

from different sets of random numbers applied in the surface flux formulation.

Simulation data are archived as snapshots of the fluid velocity field and bulk thermodynamic variables (i.e., the temperatures, water vapor and cloud water mixing ratios) every minute. Droplet data (i.e., spectral density function for the Eulerian scheme and the superdroplet data for the Lagrangian scheme) are saved every 2 min. These data are used in the analysis presented below.

3. Results of piggybacking simulations

We start with a brief discussion of the entrainment and mixing because their representation impacts simulation results differently in the two microphysics schemes as shown below. Entrainment refers to the process of bringing environmental air into a cloud that eventually dilutes the cloud and reduces its buoyancy. Entrainment is associated with large vortical structures evident in observations (e.g., Damiani et al. 2006), high-resolution model simulations (e.g., Grabowski and Clark 1991, 1993; Brenguier and Grabowski 1993; Carpenter et al. 1998; Moser and Lasher-Trapp 2017) and apparent in a typical cauliflower-like appearance of a cumulus cloud. As shown in Carpenter et al. (1998), spatial resolution applied in simulations discussed here is sufficient to represent those structures. In a natural cloud, the entrained air merges with the cloudy air through the process of turbulent stirring (often referred to as "mixing") where the interface separating the entrained air from the original cloudy air is stretched and folded, and the initially separated air volumes are broken into smaller and smaller pieces by inertial range turbulent eddies, down to the Kolmogorov microscale (about a millimeter in typical atmospheric conditions). Processes occurring across such a range of scales can only be represented in idealized frameworks such as in Krueger et al. (1997) and Su et al. (1998). A small range of scales involved in the turbulent stirring can be represented in high-resolution dynamic cloud simulations featuring grid length of a few meters, such as in Grabowski and Clark (1993) and Sato et al. (2018).

In numerical simulations discussed here, the turbulent stirring remains unresolved. As the entrained air is brought into the cloud, the sharp interface separating it from the cloudy air is smoothed by the numerical diffusion of the advection scheme. This picture applies to all fields in the Eulerian scheme as MPDATA transports the temperature, water vapor, and one-by-one all cloud water bins. In addition to smoothing the cloud–clear air interface, independent advection of all bins may result in numerical artifacts as discussed in Ovtchinnikov and Easter (2009). For the Lagrangian scheme, the temperature and

water vapor are transported by MPDATA applying the same flow as the Eulerian scheme, whereas superdroplets are carried by the predicted flow that is interpolated to the superdroplet position. These differences in the transport are exacerbated by the representation of microphysical transformations that include droplet activation, growth, or evaporation. The following discussion includes references to these key differences.

a. Simulated cloud development

Development of the simulated cloud is illustrated in Fig. 2. Figure 2a shows evolutions of the cloud-base and cloud-top heights together with the height of the cloud water center of mass derived from the four driving thermodynamic sets (two for bins in red and two for superdroplets in blue). The cloud base and cloud top are defined as the lowest and the highest levels in all model columns with the cloud water mixing ratios larger than $0.1\,\mathrm{g\,kg^{-1}}$. Horizontally uniform surface fluxes force development of boundary layer eddies shortly after the simulation onset. The boundary layer deepens and first randomly distributed small cumuli develop after about 40 min of the simulations. The cloud field gradually deepens, in the same way regardless which scheme drives the simulation, until the uniform surface fluxes are replaced by Gaussian fluxes centered in the middle of the domain at minute 60. By then, the tallest small cumulus is over 1 km deep, and the deepest cumuli are for simulations with superdroplets driving the flow. The latter is arguably because of a smaller dilution and cloud water evaporation of those poorly resolved scattered cumuli in the Lagrangian scheme. Initial development of a single larger cloud in the center of the domain can be identified around minute 80. The cloud rapidly deepens by launching sequential turrets (or thermals) as in observations and model simulations (e.g., Carpenter et al. 1998; Damiani et al. 2006; Moser and Lasher-Trapp 2017). These turrets rise from the main body of the cloud and they collapse back after losing positive buoyancy due to entrainment and buoyancy reversal resulting from cloud water evaporation. This leads to an occasional decrease of the cloud-top rise rate evident in Fig. 2 or even a sporadic decrease of the cloud-top height. Turrets in some simulations reach the domain top by 120 min. This is why the evolution shown in Fig. 2 is truncated at minute 110. The cloud base slowly rises throughout the simulations (because of a small reduction of the near-surface relative humidity) with small differences between the four simulations. The center of mass rises similarly in all simulations until about minute 100, when one of the bin simulations starts lagging behind.

Figure 2b shows the evolution of the total condensed water mass in drivers (solid lines) and piggybackers (dashed lines) applying the same colors as in the upper panel. The panel shows that clouds formed with superdroplets driving (i.e., blue lines) feature more total cloud water than when bin microphysics drives the simulation; this is shown by the difference between blue and red solid lines. Moreover, regardless which scheme drives the simulation, the superdroplets have more condensed water as shown by the difference between solid and dashed lines. These arguably come from differences in representation of cloud water advection in the two schemes, its impact on entrainment and mixing as discussed above, and possibly on the cloud buoyancy. However, the impact on the buoyancy and thus on the cloud dynamics seems relatively small because the mean cloudy updraft shown in Fig. 2c is practically the same until about minute 100 when one of the bin simulations starts lagging behind. This suggests that the differences in the total condensate shown in the middle panel are not related to the differences in the cloud dynamics (e.g., stronger updrafts when superdroplets are driving the flow), but come from more cloud water evaporation simulated by the bin scheme.

In relation to the above discussion, it should be stressed that these differences between the two microphysics modeling approaches come from the representation of physical processes, and not from the lack of water conservation in the two schemes. In particular, representation of transport and microphysical transformations in the two microphysical schemes conserve the volume integral of the total water (i.e., the sum of water vapor and cloud water) inside the computational domain. The total water increases slightly during the simulations because of the surface latent heat flux. However, the cloud water, affected by condensation and evaporation, differs significantly between the Eulerian and Lagrangian schemes as documented in Fig. 2b.

b. Illustration of cloud simulation results

Figures 3 and 4 show distributions of the cloud water mixing ratio within a y–z plane cutting across the middle of the 3D cloud at minute 106 together with the droplet spectra at two selected locations. The figures show results from a randomly selected piggybacking simulation for the Eulerian (Fig. 3) and Lagrangian (Fig. 4) schemes. In the specific simulation selected, the Lagrangian microphysics drives the flow and Eulerian microphysics piggybacks. As expected, the cloud water distributions are similar between the two figures, with a close to adiabatic central part of the cloud below 2.5 km height and a complicated pattern resulting from entrainment aloft. Because of the small number of superdroplets per grid box, the Lagrangian results shown in Fig. 4 were smoothed by calculating the droplet distribution and cloud water mixing ratio using 8 neighboring grid boxes (i.e., i and $i + 1$ in the x direction, j and $j + 1$ in the y direction, k and $k + 1$ in the vertical). This reduces the noise resulting from statistical fluctuations of the superdroplet number per grid box. However, the Lagrangian results still feature more small-scale fluctuations than the Eulerian scheme. As discussed above, the physical space advection in the bin scheme provides a significant smoothing of the cloud water field. Smoothing bin results in the same way as superdroplet results in Fig. 4 leads to hardly noticeable differences between Fig. 3 and its smoothed version (not shown).

Figures 3 and 4 also show droplet spectra at two locations near the center of the cloud, one at the height of 2 km (i.e., near the cloud bottom) and the second one at the height of 4.75 km in the upper part of the cloud. The spectra near the bottom feature almost exactly the same cloud water mixing ratio (around $1.95\,\mathrm{g\,kg^{-1}}$, not far from the adiabatic value), and the mean radius is similar in both, around 7.5 μm. However, the bin spectrum is wider than the one derived from the Lagrangian scheme. This has been argued in Morrison et al. (2018) to result from the combination of the vertical advection of droplet bins

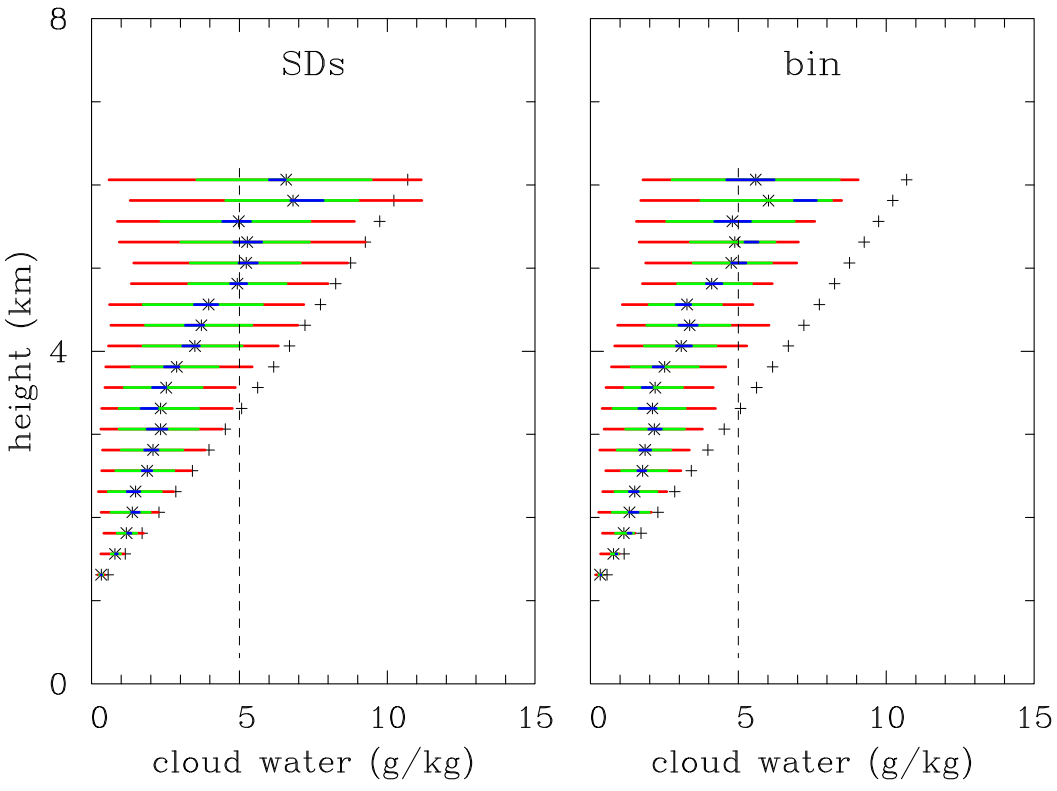

FIG. 7. Cloud water mixing ratio statistics vs height for a simulated cumulus at minute 106. Only cloudy points with the cloud water mixing ratio larger than 0.1 g kg^{-1} for both schemes are included. Every fourth model level is shown including levels where there are at least 20 data points. Thick horizontal lines show cloud water distribution percentile ranges at a given height. Red is for 10th–90th, green is for 25th–75th, and blue is for 45th–55th. Asterisks show the mean values at each height. Results are from (left) the superdroplet microphysics and (right) the bin microphysics. The dashed line at 5 g kg^{-1} mixing ratio is added to allow a better comparison between superdroplet and bin results. Plus symbols show the adiabatic cloud water mixing ratios.

in a stratified environment and advection in the radius space that represents diffusional growth of cloud droplets; see also Fig. 3 in Grabowski et al. (2019). The spectra in the upper part of the cloud are also similar and feature a peak around 14 μm and droplets of smaller sizes to the left. Small cloud droplets may come from either evaporation of cloud water due to entrainment or from fresh activation of entrained CCN (see Brenguier and Grabowski 1993). In general, the multimodal droplet spectra in diluted cloudy volumes agree with numerous cumulus observations starting with Warner (1969). The cloud water is significantly below the adiabatic value (around 8 g kg^{-1} at this height) for both schemes and about 20% smaller for the bin scheme. The former is consistent with cloud dilution aloft and the latter agrees with more dilution simulated by the bin scheme as shown in Fig. 2b. The reduced cloud water in the bin scheme results in the smaller mean radius (11 vs 12 μm) as shown in the figures. The bin spectrum is smoother and reaches larger droplet sizes than the one derived from the Lagrangian scheme.

c. *Statistical comparison between the two schemes*

To illustrate results from all piggybacking simulations, Figs. 5 and 6 show evolutions of the cloud water and droplet number mixing ratios together with the mean droplet radius and spectral width for bin and superdroplet simulations, respectively. The two figures show results at the height of 4 km, that is, in the upper half of the cloud depth. Both drivers and piggybackers are used in the figures which explains why four datasets are used in both figures. Comparing the two figures shows that the mean quantities (shown by stars in the figures) evolve similarly in the two schemes, with small differences between individual realizations. Notable differences include the spectral width, significantly larger in the bin scheme, slightly smaller cloud water mixing ratios for the bin scheme (in agreement with Figs. 2–4), and larger percentile ranges for the superdroplets, especially for the spectral width. Of notice are also larger number mixing ratios in the Lagrangian scheme. This is because of the upward adjustment of the droplet concentration in the Lagrangian scheme that was explained in G20 as follows: If a grid box features a smaller number of superdroplets because of a statistical fluctuation, additional superdroplets can be created to increase the droplet concentration toward the activation limit. At the same time, a grid box with a larger number of superdroplets (even above the activation limit) remains unchanged. As a result, Twomey activation always adjusts upward the number of superdroplets and this leads

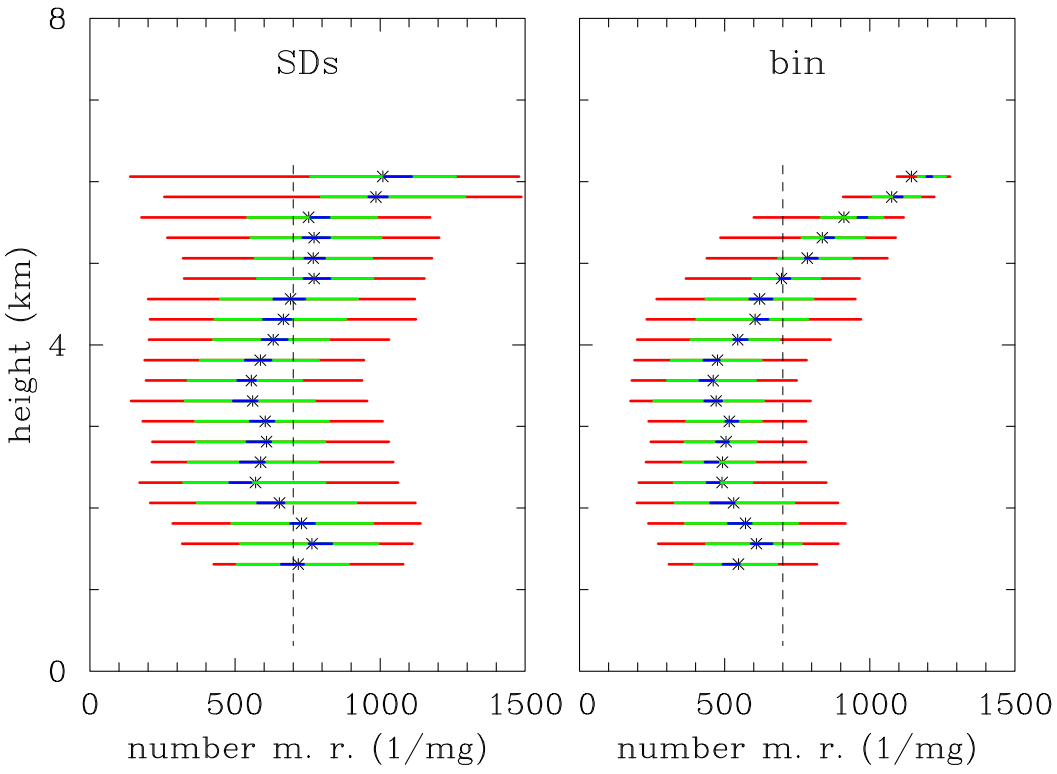

FIG. 8. As in Fig. 7, but for the droplet number mixing ratio. The dashed line at 700 mg^{-1} is added to allow a better comparison between superdroplet and bin results.

to a higher on average droplet concentration when compared to the bin microphysics.[2] The top two panels in both figures show a small decrease of the mixing ratios in time that may come from the simulated clouds progressing through their life cycle.

Figures 7–10 show statistics of cloud parameters as a function of height for the two schemes at minute 106 of the piggybacking simulation used in Figs. 3 and 4. Figure 7 shows the cloud water mixing ratio statistics. Both schemes show a large scatter of the mixing ratio in agreement with aircraft observations (e.g., Warner 1955; Blyth and Latham 1985; Burnet and Brenguier 2007; Gerber et al. 2008). The mean values at a given height are slightly smaller in the bin scheme. But there are also clear differences. First, in agreement with Figs. 3–6, the variability of the mixing ratio is larger for the superdroplets, especially in the upper half of the cloud depth. This is because of statistical fluctuations due to a relatively small number of superdroplets per grid box used in the simulations. Second, the 90th percentiles above 3 km in the bin scheme reach only values significantly smaller than the adiabatic value, and the 10th percentiles are smaller in the Lagrangian scheme. These differences likely come from the contrast in the representations of droplet transport and evaporation resulting from the small-scale homogenization as discussed above. Statistical fluctuations of the superdroplet number per grid box in the Lagrangian scheme allow 90th-percentile-reaching adiabatic values. This problem is reduced when a larger number of superdroplets is used as illustrated in section 4.

Droplet number mixing ratio statistics are compared in Fig. 8. As in the cloud water case, the number mixing ratio variability is larger for the superdroplets (cf. Figs. 5 and 6). The mean values increase with height in the upper part of the cloud depth. This is likely because of the in-cloud CCN activation in the upper parts of the cloud that feature higher vertical velocities (not shown). Larger mean number mixing ratios in the Lagrangian scheme are because of the upward adjustment of the droplet concentration in the superdroplet activation. The problem becomes less significant when the number of superdroplets is increased. For the bin microphysics, advecting each bin separately in the physical space can also lead to some unphysical behavior of the total droplet concentration (see Ovtchinnikov and Easter 2009).

Figure 9 shows similar statistics for the mean droplet radius. The average mean radii are similar between the two schemes below 4 km, with the range between 6 and 9 μm. This range is similar to the observations of shallow warm cumuli over Montana; see Fig. 9 in Jensen et al. (1985). Above 4 km, the average mean radius is larger and the 90th percentile is significantly larger in the Lagrangian scheme. The reason is

[2] Note that the same problem exists with traditional superdroplets, that is, when superdroplets represent unactivated CCN and activated cloud droplets as in Shima et al. (2009). This is because droplet concentration can only increase according to the superdroplet multiplicity.

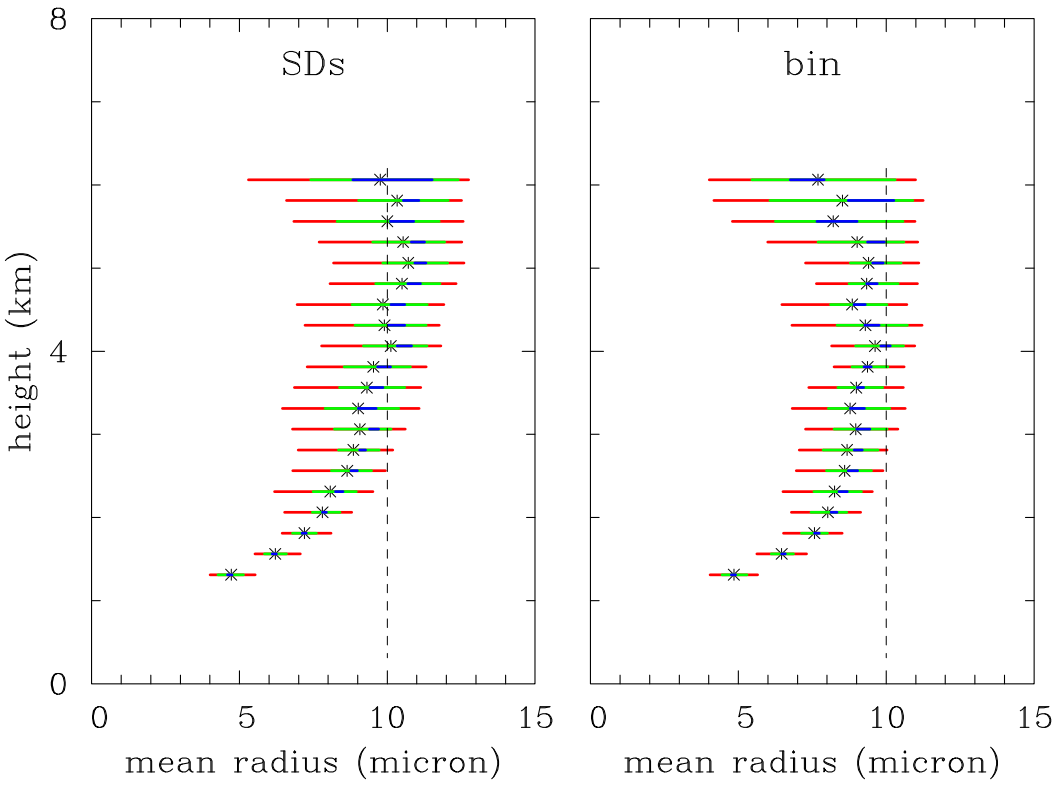

FIG. 9. As in Figs. 7 and 8, but for the droplet mean radius. The dashed line at 10-μm radius is added to allow a better comparison between superdroplet and bin results.

likely a combination of the numerical diffusion in the bin scheme (that leads to smaller cloud water mixing ratios in the upper part of the cloud, cf. Figs. 4–6) and the impact of the "eddy hopping" mechanism as argued in Grabowski and Abade (2017) and Abade et al. (2018); see discussion in LT05 (Fig. 6 in particular) and in Grabowski and Wang (2013). Eddy hopping refers to a mechanism in which individual droplets follow different trajectories in a turbulent flow and experience different growth histories (Cooper 1989). One can argue that the eddy hopping by the resolved flow can be simulated in both Lagrangian and Eulerian schemes. However, differences of the droplet transport and of the representation of droplet growth/evaporation makes such an argument questionable. The increasing-with-height 10th–90th-percentile range is similar between the two schemes.

Statistics of the spectral width are shown in Fig. 10. The simulated width shows the largest difference between the two schemes. The width decreases within the first few hundred meters above the cloud base in both schemes. This is expected within the adiabatic or nearly adiabatic cloud volumes because droplet size distribution narrows when the volume rises away from the cloud base. However, spectral widths in the Lagrangian scheme are about half of that for the Eulerian scheme. This should not be surprising as the spectral bin resolution has the largest impact on the predicted spectral width when droplets are small. However, the bin mean spectral widths are significantly larger than for the Lagrangian scheme across the entire cloud depth. This agrees with the argument presented in Morrison et al. (2018) that bin advection in the stratified atmosphere combined with advection in the bin space typically results in artificial spectral broadening. The 10th–90th-percentile range is much larger for the Lagrangian scheme. This may come from a relatively small number of superdroplets in current simulations, but this conclusion holds when more superdroplets are used (see section 4). For the Lagrangian scheme, specific values of the spectral width, between 1 and 3 μm throughout most of the cloud depth, is consistent with the spectral width observed in Montana shallow cumuli (Fig. 10 in Jensen et al. 1985). The range of mean radii (5–10 μm) and corresponding spectral widths (1–4 μm) across the cloud depth in Figs. 9 and 10 for the Lagrangian scheme is in a better agreement with observations of monsoon convection over Indian subcontinent reported in Prabha et al. (2012, see Fig. 6 therein). LT05 show examples of the simulated droplet spectra at 4.2-km height (see Figs. 14 and 15 and Table 1 therein) with the radius spectral width between 2.0 and 3.5 μm and the mean droplet radius between 6 and 9 μm. Such spectral widths also agree better with the Lagrangian scheme results.

d. Comparison facilitated by piggybacking

As an introduction, Fig. 11 compares point-by-point bulk thermodynamic variables, the temperature, water vapor and cloud water mixing ratios, and the resulting buoyancy in cloudy

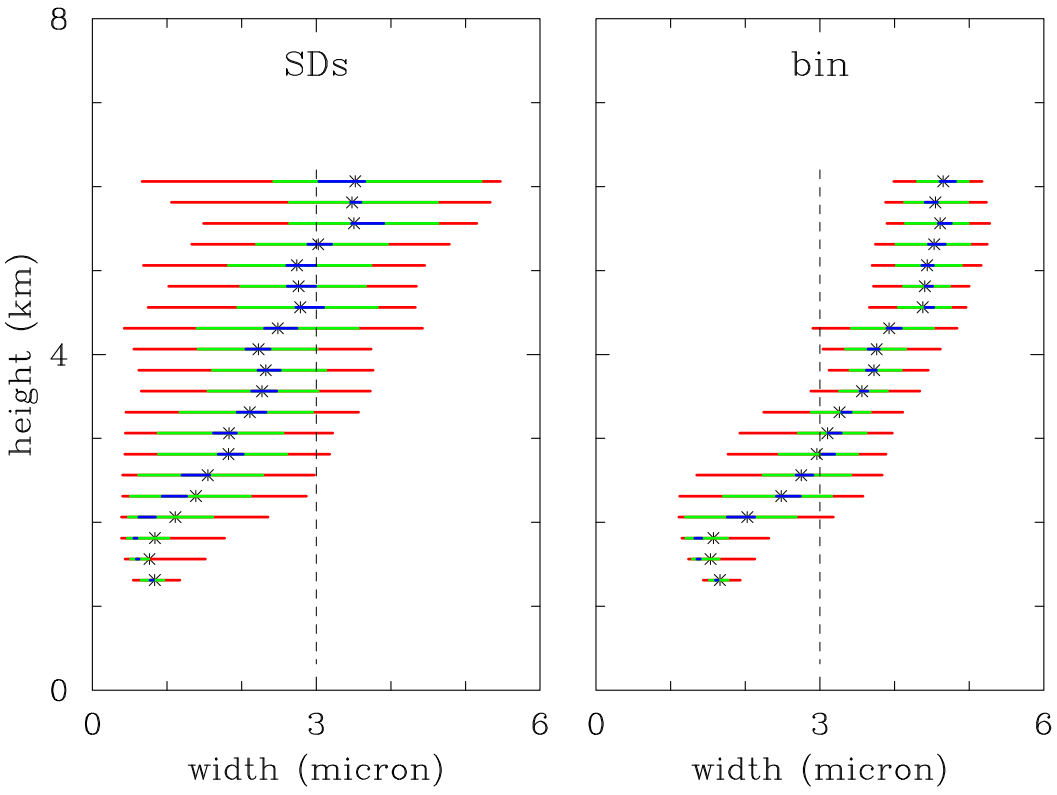

FIG. 10. As in Figs. 7–9, but for the spectral width. The dashed line at 3-μm width is added to allow a better comparison between superdroplet and bin results.

grid boxes at minute 106 of the same simulations as in the previous figures. Blue, red, and green symbol colors show the height the data come from. The buoyancy is defined by the deviation of the density potential temperature from that of the environment [see 4a in Grabowski and Smolarkiewicz (2002) and accompanying discussion; the density potential temperature θ_d is defined as $\theta_d = \theta(1 + \varepsilon q_v - q_c)$ where θ is the potential temperature, q_v is the water vapor mixing ratio, q_c is the cloud water mixing ratio, and $\varepsilon = R_v/R_d - 1$; R_v and R_d are the gas constants for water vapor and dry air, respectively]. The comparison in Fig. 11 is only possible through piggybacking because each grid box has two sets of thermodynamic variables and each symbol in the figure compares point-by-point variables from the two sets. The figure shows that the temperature and water vapor mixing ratio are close in both sets with a few exceptions. This is expected because the two variables come from solving exactly the same equations with the only difference being the condensation/evaporation term. In contrast, the cloud water mixing ratio can differ significantly, especially away from the cloud base (red and green colors). Point-by-point fluctuations of the cloud water is a combination of numerical diffusion for the bin scheme and statistical fluctuations of the superdroplet number in a grid box for the particle-based scheme. Because condensation of 1 g kg^{-1} of water vapor increases the temperature by about 2 K, small spread of the temperature and water vapor implies that the differences in the cloud water mixing ratio are not systematic (i.e., long lasting) because then the temperature and water vapor spread would be larger. There seems to be more points below the one-to-one line for cloud water larger than 2 g kg^{-1}. This shows that the Lagrangian microphysics feature higher cloud water mixing ratios away from the cloud base, in agreement with results shown previously. The differences in the cloud water lead to a scatter in the buoyancy above 2.5 km as show by the red and green colors. There seem to be more data points below the one-to-one line which suggests that the Lagrangian microphysics feature slightly more cloud buoyancy. Figures for different simulations and at different times look similar to Fig. 11 (not shown).

The format of Fig. 11 is used to compare point-by-point microphysical characteristics simulated by the two microphysical schemes in Fig. 12. As in Fig. 11, the figure applies blue, red, and green colors to show the height data come from. The upper panel compares point-by-point droplet number mixing ratio statistics. As for the cloud water, there is a significant scatter. In the Lagrangian scheme, the small number of superdroplets per grid box together with the way Twomey activation is implemented leads to the apparent pattern where droplet number mixing ratio can only change in a discontinuous way. In contrast, the bin scheme does not have such a limitation, although numerical issues (e.g., Ovtchinnikov and Easter 2009) likely contribute to the scatter as well. The blue color shows that number mixing ratios are typically larger for the Lagrangian microphysics

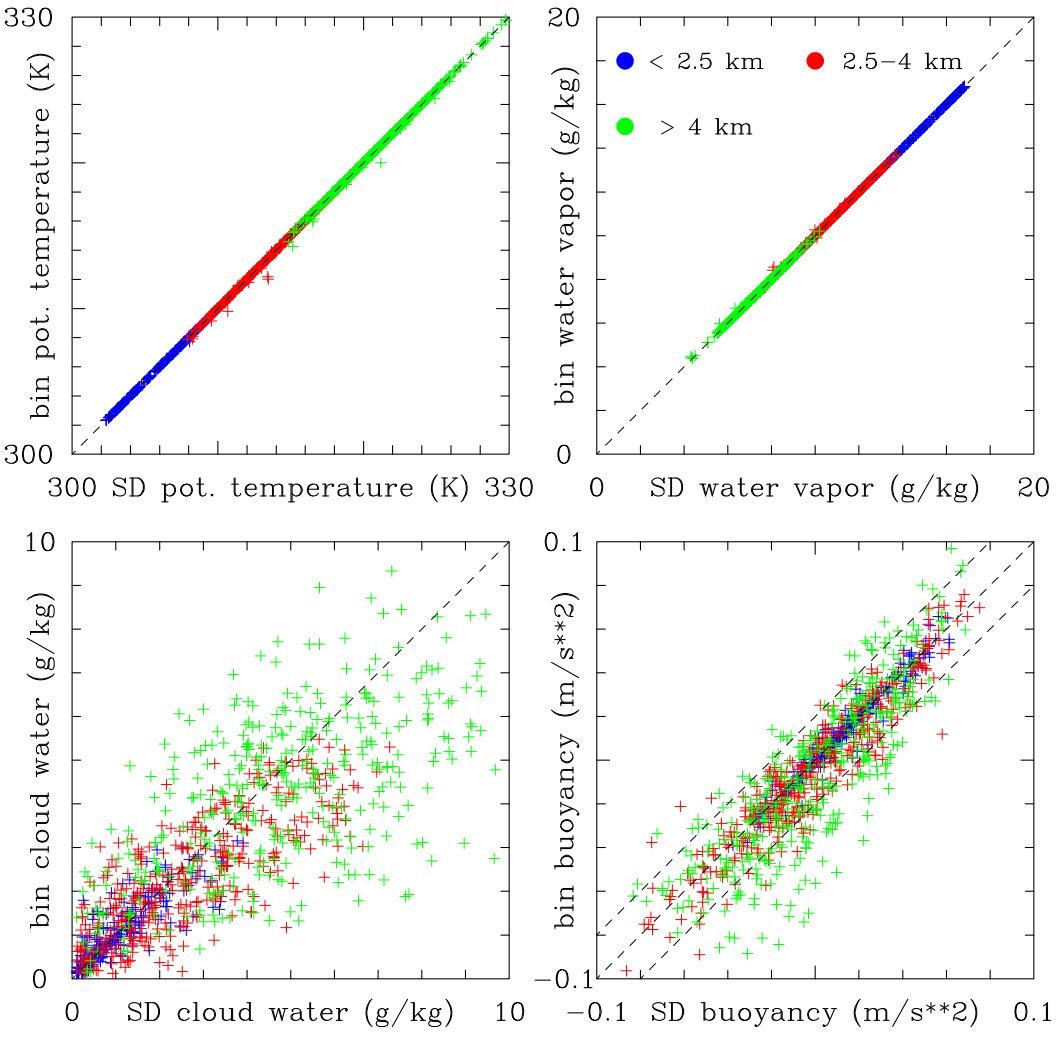

FIG. 11. Point-by-point comparison of model fields at all cloudy points at minute 106 from the same simulations as Figs. 3–8. (top left) Potential temperature, (top right) water vapor mixing ratio, (bottom left) cloud water mixing ratio, and (bottom right) buoyancy. Superdroplet and bin variables are shown on the horizontal and vertical axes, respectively. Only 5% of all data points is shown for clarity. The dashed line along the diagonal shows the perfect agreement between the two schemes. In the bottom-right panel, additional two lines show deviations of 0.02 m s^{-2} from the diagonal. Blue, red, and green symbols are for grid volume below 2.5 km, between 2.5 and 4.0 km, and above 4.0 km, respectively, as shown in the top-right panel.

below 2.5 km, and the opposite is true for cloudy volumes above 4 km (the green points), that is, in more diluted upper parts of the cloud.

The mean radii predicted by the two schemes are compared in Fig. 12b. Except for some outliers, the mean radii are relatively close between the two schemes below 2.5 km (blue color). The comparison deteriorates at higher levels, with red symbols scattered approximately symmetric around the one-to-one line, and green symbols (data points above 4 km) typically located below the one-to-one line. The systematic differences at the large mean radius end, that is, in weakly diluted regions near the cloud top, come from the underprediction of the cloud water mixing ratio in the bin scheme as discussed before.

Finally, Fig. 12c shows the comparison of the spectral width. Most of the points are located above the one-to-one line implying that the spectral width in the bin scheme is typically larger, and often significantly larger, than in the superdroplet scheme. This is true throughout the cloud depth as illustrated by the symbol colors. The systematic difference between the Lagrangian and Eulerian spectral width is consistent with results already shown in Figs. 5, 6, and 10, and with the impact of numerical problems in the bin scheme as discussed in Ovtchinnikov and Easter (2009) and Morrison et al. (2018). The cluster of blue points with a small spectral width in the lower left corner and away from the one-to-one line comes from volumes not far from the cloud base where droplets are small and the bin resolution in the Eulerian scheme is never

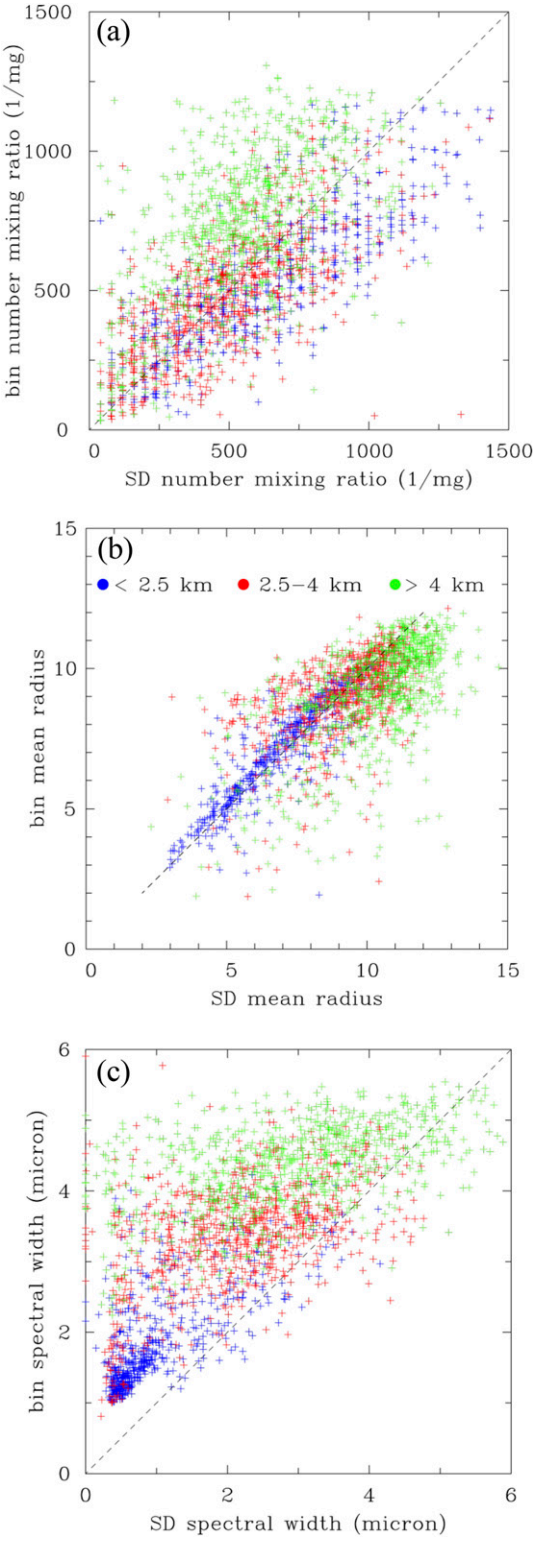

FIG. 12. As in Fig. 11, but for (a) number mixing ratio, (b) mean radius, and (c) spectral width. Blue, red, and green symbols are for grid volume below 2.5 km, between 2.5 and 4.0 km, and above 4.0 km, respectively, as shown in (b).

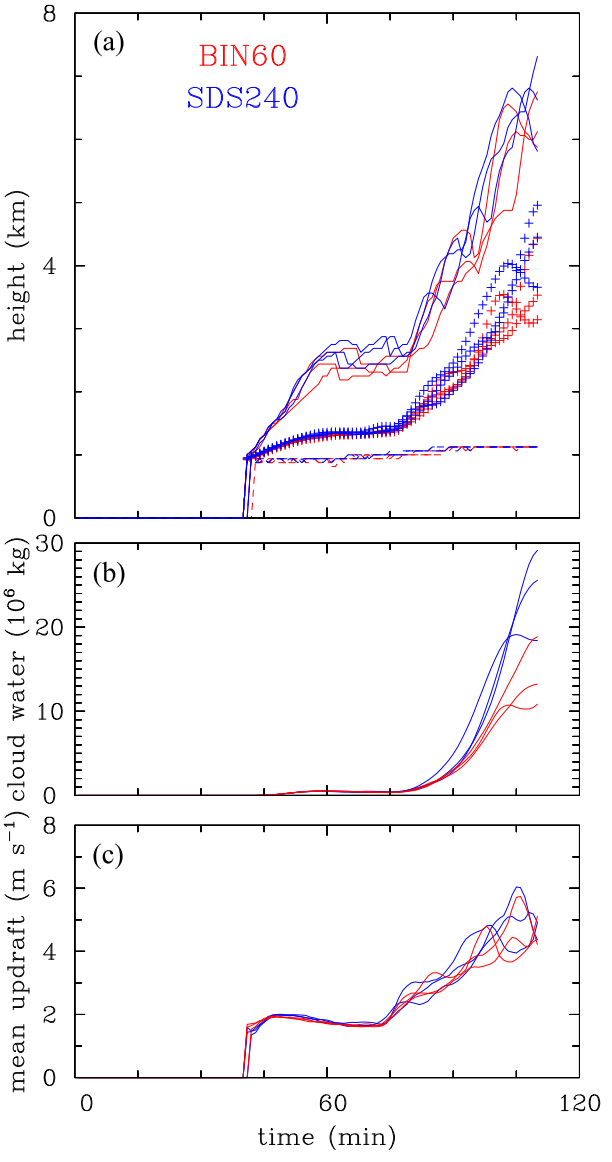

FIG. 13. As in Fig. 2, but for BIN60 (red) and SDS240 (blue) simulations.

sufficient. There are also some points where the spectral width is lager in the Lagrangian scheme, that is, those below the one-to-one line. These arguably come from the broadening of the droplet spectrum resulting from individual droplets following different trajectories and experiencing different growth histories (i.e., the eddy hopping mechanism; Cooper 1989; LT05; Grabowski and Abade 2017; Abade et al. 2018).

4. Sensitivity simulations

Six sensitivity simulations without piggybacking, three applying Eulerian microphysics and three with the Lagrangian scheme, have been completed. For the Eulerian microphysics,

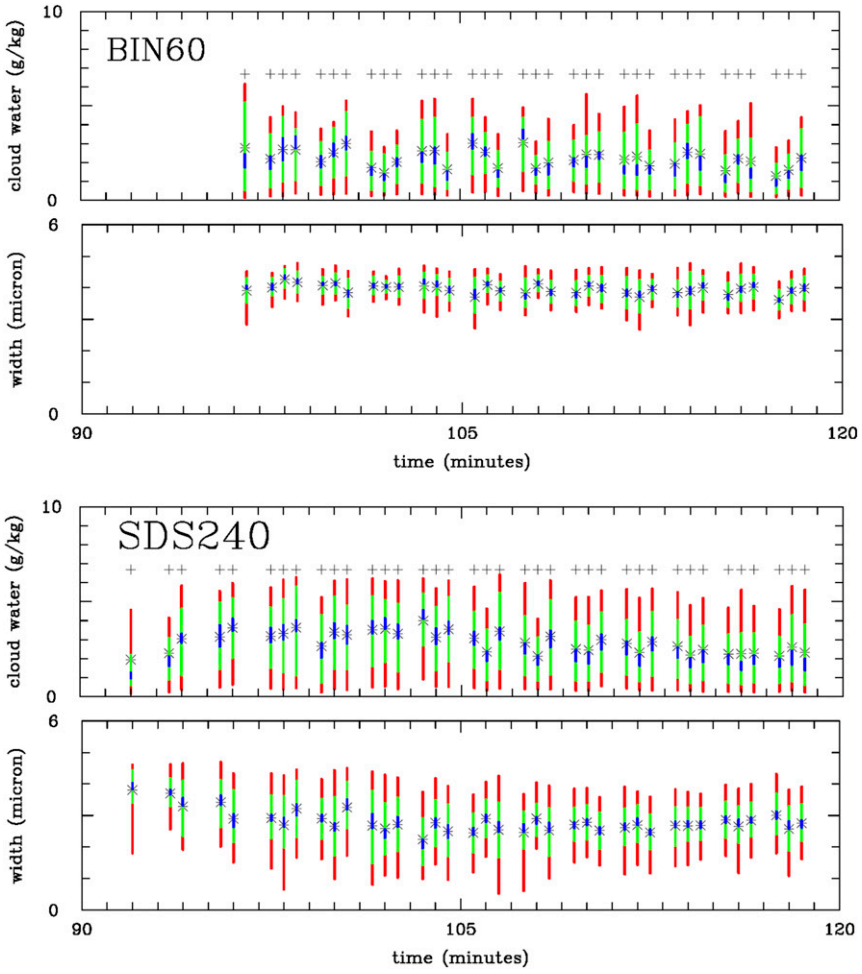

FIG. 14. Evolutions of BIN60 and SDS240 set results at 4-km height sampled and presented as in Figs. 5 and 6. The panels show the mean liquid water mixing ratio and mean spectral width only. Only cloudy points with the cloud water mixing ratio larger than 0.1 g kg^{-1} are included. Thick lines show cloud percentile ranges: red is for 10th–90th, green is for 25th–75th, and blue is for 45th–55th. Asterisks show the mean values at each height and plus symbols show the adiabatic cloud water. Results are shown every 2 min with individual sets shown shifted from the actual minute for clarity.

the number of bins is increased from 30 to 60, and the bin size is reduced from 0.7 to 0.35 μm. These simulations are referred to as BIN60. For the Lagrangian microphysics, the number of superdroplets per grid box is increased from 30 to 240 implying that superdroplets are activated in installments of $N_{max}/240$ (see section 2b). These simulations are referred to as SDS240.

Overall, cloud evolution in the six simulations are similar to the piggybacking simulations. This is illustrated in Fig. 13 in a similar format as Fig. 2. The scatter between evolutions of the cloud top and center of mass in Fig. 13 is larger than in Fig. 2, with Lagrangian microphysics showing typically the highest cloud top and the highest center of mass among all realizations. The total cloud water evolutions are also similar to those in Fig. 2, although the difference between Eulerian and Lagrangian microphysics seems larger despite the scatter. One can argue that increasing the number of superdroplets should improve the Lagrangian simulation because the amplitude of statistical fluctuations is reduced. On the other hand, increasing the number of bins in the Eulerian scheme can either improve or degrade the simulation. The improvement can come from a better resolution in the bin space and thus reducing the impact of the numerical diffusion when representing condensation/evaporation (e.g., Grabowski et al. 2011). However, the bin width is already small with 30 bins in the piggybacking simulations, especially when comparing to a few dozen bins applied in simulations of precipitating clouds (e.g., Table 3 in Khain et al. 2015). Those bin schemes typically have less than a dozen bins in the range considered here. On the other hand, increasing the number of bins imply that more bins need to be advected in the physical space and thus increasing the potential for numerical problems as discussed in

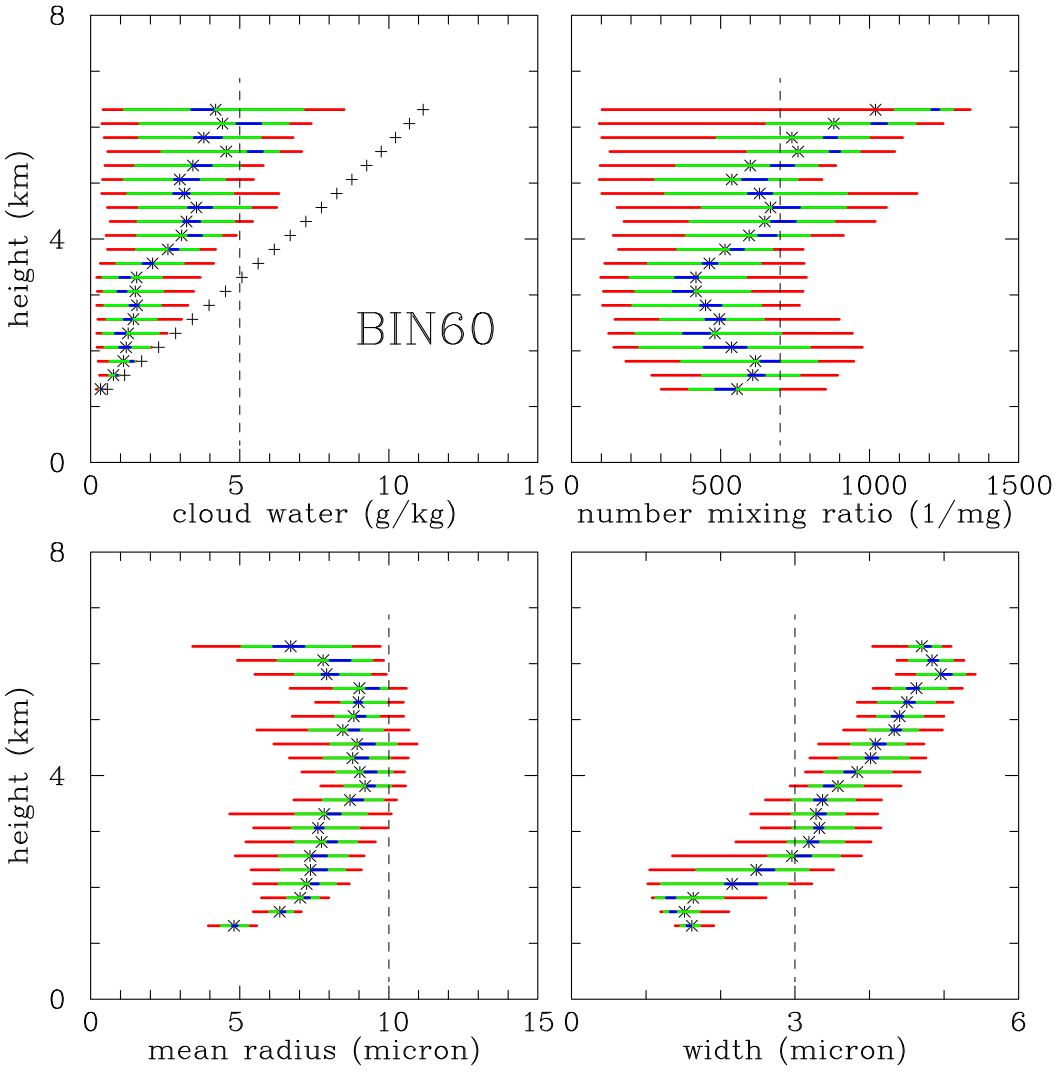

FIG. 15. As in Figs. 7–10, but for BIN60 simulation at minute 108.

Ovtchinnikov and Easter (2009) and Morrison et al. (2018). The mean vertical velocity in the bottom panel also shows more fluctuations when compared to Fig. 2 and does not seem to unambiguously explain clear differences in the total cloud water.

Figure 14 shows evolutions of the cloud water mixing ratio and spectral width statistics at 4 km for all BIN60 and SDS240 simulations in the same format as Figs. 5 and 6. Comparing the BIN60 results with Fig. 5 shows a small impact of the increased number of bins on the evolutions of the cloud water and spectral width. For the Lagrangian scheme (i.e., SDS240 and Fig. 6), there are larger differences. The 90th percentile for the cloud water between minutes 100 and 110 are further away from the adiabatic values. The 10th–90th-percentile range for the spectral width is reduced (especially for the last 10 min of the simulations), and the mean spectral width is slightly increased in SDS240 when compared to Fig. 6. As in piggybacking simulations, the mean cloud water mixing ratio is lower in BIN60 than in SDS240, especially between minutes 100 and 110.

As in the piggybacking case, we randomly selected two simulations, one with the Eulerian and one with the Lagrangian microphysics. For the two simulations, we decided to use minute 108, with clouds reaching slightly higher than in the piggybacking simulations at minute 106 shown in previous figures. BIN60 and SDS240 can be compared as in Figs. 7–10 keeping in mind that comparison is for two different cloud simulations. The results are presented in Fig. 15 for BIN60 and Fig. 16 for SDS240.

Comparing Fig. 15 with the corresponding panels of Figs. 7–10 documents the impact of the number of bins in the Eulerian scheme. The percentile ranges for the droplet number mixing ratio are larger than in the original piggybacking simulations, with the increase mostly at the low percentile range and in the upper part of the cloud. This is also true in the two other bin simulations and for different times in the simulation selected

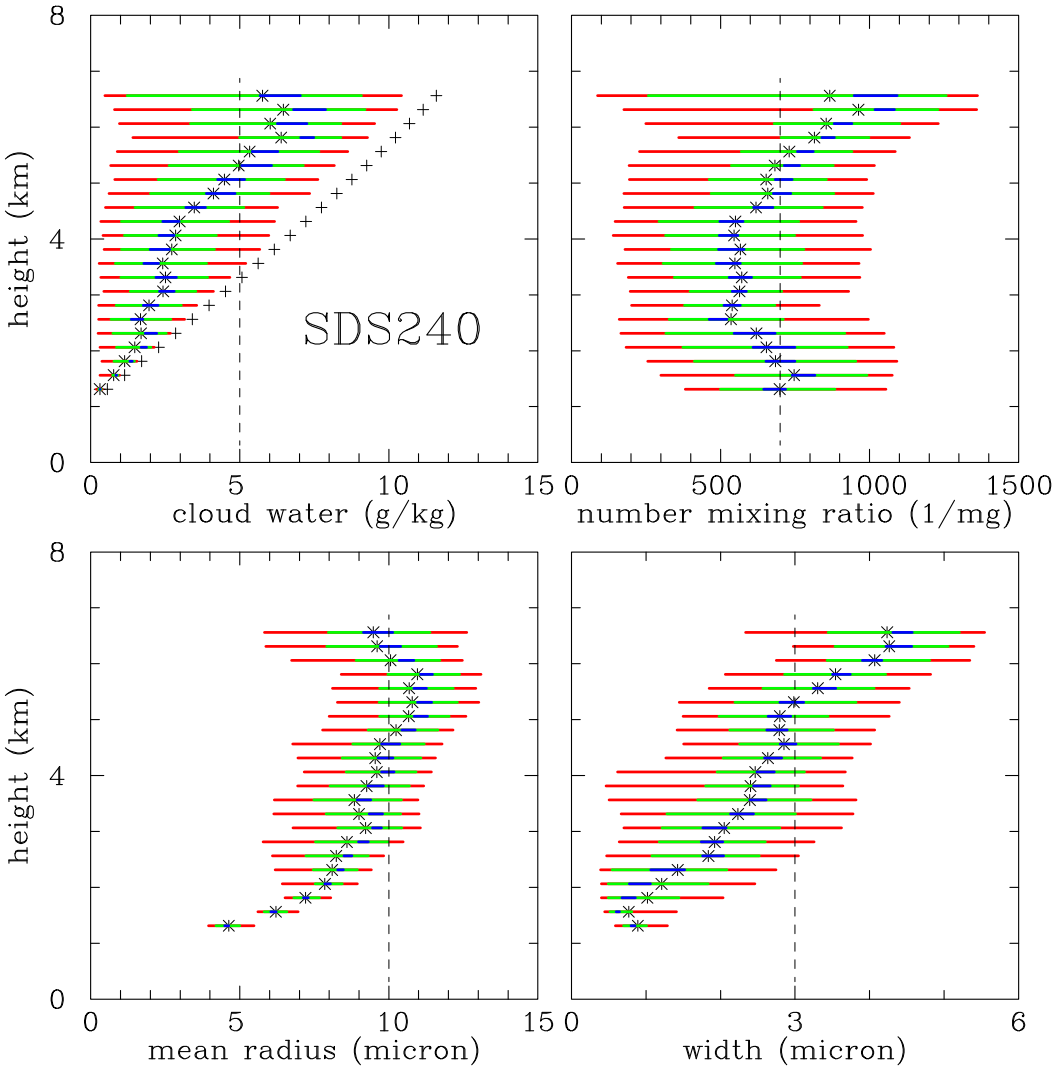

FIG. 16. As in Fig. 15, but for SDS240 simulation at minute 108.

for the Fig. 15 (not shown). Another difference, also true for other simulations, is a more rapid increase of the spectral width above the cloud base. The width reaches 3 microns around 3 km in Fig. 10, and about 0.5 km lower in Fig. 15. Arguably, this comes from the necessity to transport more bins in the physical space (60 in BIN60 versus 30 in the piggybacking simulations) as discussed above.

Comparing the panels in Fig. 16 with the left panels of Figs. 7–10 documents that fourfold increase of the number of superdroplets has a relatively minor impact. The 90th percentile of the cloud water mixing ratio no longer exceeds the adiabatic value, droplet number mixing ratio and its percentile variability are practically unchanged, so is the mean radius. The mean spectral width does not change either, although the 10th–90th-percentile range is reduced. This suggests that increasing the mean number of superdroplets per grid volume beyond 30 in the nonprecipitating case provides only small changes to the results.

5. Discussion and conclusions

Following G20, this manuscript reports modeling results that compare Eulerian bin microphysics and Lagrangian particle-based microphysics in simulations of a warm nonprecipitating cumulus. The Eulerian bin microphysics is a traditional approach to simulate droplet spectra applying the spectral density function. The Lagrangian particle-based microphysics is a novel methodology that gains popularity because of its benefits when compared to the bin microphysics (see discussion in Grabowski et al. 2019). We apply a simulation setup of LT05 that leads to a development of a single cumulus congestus in the center of the computational domain. LT05 applied a cumbersome methodology of combining bulk microphysics cloud simulation with Lagrangian trajectories to predict droplet spectra at selected locations inside a simulated cloud and to demonstrate the impact of different droplet ensemble trajectories through a turbulent cloud on the droplet spectra

as suggested by Cooper (1989). The Lagrangian methodology automatically provides similar outcome as pointed out in Grabowski et al. (2019, see Fig. 5 therein and its discussion). The simulations presented here apply implicit large-eddy simulation methodology and purposely excluded representation of subgrid-scale processes. This is because those processes cannot be represented in the same way in Eulerian and Lagrangian approaches. Grabowski and Abade (2017) argued that the Lagrangian particle-based microphysics constitutes a simulation methodology for which a physically consistent subgrid-scale scheme can be designed; see also Hoffmann et al. (2019). Development of such a multiscale scheme is difficult, maybe even impossible, for the Eulerian bin microphysics. To allow a point-by-point comparison between the two schemes, the piggybacking technique is applied with the two schemes operating side-by-side in a single simulation. One scheme is used to calculate buoyancy and thus it drives the simulated flow, and the second scheme piggybacks the predicted flow without affecting it. A small ensemble of simulations is completed, with two simulations driven by the bin microphysics and two by the particle-based microphysics. Clouds in four simulations develop similarly, but there are obvious differences (such as cloud appearance at a particular time) that supports the need for the piggybacking approach.

There are two key differences between the Eulerian and Lagrangian simulation results. First, Eulerian simulations feature reduced cloud water mixing ratio in diluted upper parts of a simulated cloud. As a result, the total cloud water mass differs significantly at the end of the simulations. We argue that this comes from the difference in the representation of the droplet physical space transport in the two schemes and how it affects the simulation of mixing resulting from entrainment of subsaturated environmental air. One can argue that the total cloud water difference may also come from a dynamical impact, for instance, presence of stronger updrafts resulting from buoyancy differences that can lead to more condensation and thus more cloud water. However, the mean cloud updraft velocities are similar in all simulations and thus do not support such a conjecture. In essence, the difference in the total cloud water seems to come from the thermodynamics (e.g., cloud water evaporation) and not from the dynamics.

Second, bin microphysics simulates significantly larger spectral widths than those simulated by the Lagrangian microphysics. Applying piggybacking methodology demonstrates this in an unequivocal way; see Fig. 12. The simulated spectral width is the most significant microphysical difference between the two cloud simulation methodologies. The fact that the cloud chamber simulations in G20 did not reveal this problem implies that the culprit is in the coupling between the vertical advection in the stratified environment (that provides the supersaturation source) and the droplet growth as suggested in Morrison et al. (2018); see also Fig. 3 in Grabowski et al. (2019). Increasing the number of bins in the sensitivity simulations provides no improvement. This is perhaps because of compensating effects of the increase of the number of bins that need to be advected in the physical space (that increases the potential for numerical artifacts) and the reduction of the bin size that improves accuracy of the spectral change calculation. Overprediction of the spectral width in the bin scheme has likely implications for the modeling of rain formation, an aspect that needs to be investigate in the future.

G20 mention that the computational cost of the bin and superdroplet cloud chamber simulations are comparable, with the 40-per-gridbox superdroplet simulations requiring about 25% more computational time than 40-bin Eulerian simulations. The difference is significantly larger in simulations discussed here. For instance, test simulations with 151^3 grid and 30 superdroplets per grid box required about *3 times less* computational time than similar bin simulation with 30 bins. The SDS240 simulation required over *5 times less* computational time when compared to BIN60. The key difference with G20 is the ratio between the volume of the cloud and the computational domain volume, the cloud volume fraction. The fraction was close to one in G20 (because the cloud fills almost entire chamber) and is typically below 10% here. For Lagrangian microphysics, the cloud volume fraction matters because superdroplets exist only inside the cloud when Twomey activation is used (Grabowski et al. 2018). In contrast, the cloud volume fraction does not matter for the bin microphysics because computational effort of each bin advection in the physical space is independent of the cloud fraction. However, as pointed out in Grabowski et al. (2018), such argument may not apply to parallel calculations because load imbalances need to be considered.

The simulations presented in this paper should be consider as a pilot investigation. As a next step, one should systematically explore the role of the spatial resolution in the physical space in connection to the bin resolution for the Eulerian scheme and the number of superdroplets in the Lagrangian scheme. Some of such studies already exist in the literature, for instance, those considering the number of superdroplets (e.g., Arabas and Shima 2013; Grabowski et al. 2018; Hoffmann et al. 2019; G20) or the spatial resolution for simulations of shallow convection (e.g., Stevens et al. 2002; Matheou et al. 2011; Sato et al. 2018). For the bin microphysics, higher spatial resolution seems to provide less spectral spreading as suggested in Morrison et al. (2018). However, the impact of all those factors combined in piggybacking simulations with the two schemes is unclear and should be investigated in follow-up studies including droplet collisions. We hope to report on some of such studies in the future.

Acknowledgments. This manuscript was written in March and April and revised in June, July, and August 2020 during NCAR's compulsory work-from-home period due to the COVID-19 pandemic. The author acknowledges partial supported from the U.S. DOE ASR Grant DE-SC0016476. Comments on an early draft by Drs. Hanna Pawlowska and Shin-ichiro Shima are acknowledged. Insightful comments from the three reviewers led to the final version of this manuscript. NCAR is sponsored by the National Science Foundation.

REFERENCES

Abade, G. C., W. W. Grabowski, and H. Pawlowska, 2018: Broadening of cloud droplet spectra through eddy hopping:

Turbulent entraining parcel simulations. *J. Atmos. Sci.*, **75**, 3365–3379, https://doi.org/10.1175/JAS-D-18-0078.1.

Andrejczuk, M., W. W. Grabowski, S. P. Malinowski, and P. K. Smolarkiewicz, 2004: Numerical simulation of cloud–clear air interfacial mixing. *J. Atmos. Sci.*, **61**, 1726–1739, https://doi.org/10.1175/1520-0469(2004)061<1726:NSOCAI>2.0.CO;2.

——, J. M. Reisner, B. Henson, M. K. Dubey, and C. A. Jeffery, 2008: The potential impacts of pollution on a nondrizzling stratus deck: Does aerosol number matter more than type? *J. Geophys. Res.*, **113**, D19204, https://doi.org/10.1029/2007JD009445.

——, W. W. Grabowski, J. Reisner, and A. Gadian, 2010: Cloud-aerosol interactions for boundary-layer stratocumulus in the Lagrangian cloud model. *J. Geophys. Res.*, **115**, D22214, https://doi.org/10.1029/2010JD014248.

Arabas, S., and S. Shima, 2013: Large-eddy simulations of trade wind cumuli using particle-based microphysics with Monte Carlo coalescence. *J. Atmos. Sci.*, **70**, 2768–2777, https://doi.org/10.1175/JAS-D-12-0295.1.

——, A. Jaruga, H. Pawlowska, and W. W. Grabowski, 2015: Libcloudph11 0.2: Single-moment bulk, double-moment bulk, and particle-based warm-rain microphysics library in C++. *Geosci. Model Dev.*, **8**, 1677–1707, https://doi.org/10.5194/gmd-8-1677-2015.

Blyth, A. M., and J. Latham, 1985: An airborne study of vertical structure and microphysical variability within a small cumulus. *Quart. J. Roy. Meteor. Soc.*, **111**, 773–792, https://doi.org/10.1002/qj.49711146907.

Brenguier, J.-L., and W. W. Grabowski, 1993: Cumulus entrainment and cloud droplet spectra: A numerical model within a two-dimensional dynamical framework. *J. Atmos. Sci.*, **50**, 120–136, https://doi.org/10.1175/1520-0469(1993)050<0120:CEACDS>2.0.CO;2.

——, and L. Chaumat, 2001: Droplet spectra broadening in cumulus clouds. Part I: Broadening in adiabatic cores. *J. Atmos. Sci.*, **58**, 628–641, https://doi.org/10.1175/1520-0469(2001)058<0628:DSBICC>2.0.CO;2.

Burnet, F., and J.-L. Brenguier, 2007: Observational study of the entrainment-mixing process in warm convective clouds. *J. Atmos. Sci.*, **64**, 1995–2011, https://doi.org/10.1175/JAS3928.1.

Carpenter, R. L., K. K. Droegemeier, and A. M. Blyth, 1998: Entrainment and detrainment in numerically simulated cumulus congestus clouds. Part I: General results. *J. Atmos. Sci.*, **55**, 3417–3432, https://doi.org/10.1175/1520-0469(1998)055<3417:EADINS>2.0.CO;2.

Clark, T. L., 1974: On modelling nucleation and condensation theory in Eulerian spatial domain. *J. Atmos. Sci.*, **31**, 2099–2117, https://doi.org/10.1175/1520-0469(1974)031<2099:OMNACT>2.0.CO;2.

Cooper, W. A., 1989: Effects of variable droplet growth histories on droplet size distributions. Part I: Theory. *J. Atmos. Sci.*, **46**, 1301–1311, https://doi.org/10.1175/1520-0469(1989)046<1301:EOVDGH>2.0.CO;2.

Damiani, R., G. Vali, and S. Haimov, 2006: The structure of thermals in cumulus from airborne dual-Doppler radar observations. *J. Atmos. Sci.*, **63**, 1432–1450, https://doi.org/10.1175/JAS3701.1.

Gerber, H. E., G. M. Frick, J. B. Jensen, and J. G. Hudson, 2008: Entrainment, mixing, and microphysics in trade-wind cumulus. *J. Meteor. Soc. Japan*, **86A**, 87–106, https://doi.org/10.2151/jmsj.86A.87.

Grabowski, W. W., 2014: Extracting microphysical impacts in large-eddy simulations of shallow convection. *J. Atmos. Sci.*, **71**, 4493–4499, https://doi.org/10.1175/JAS-D-14-0231.1.

——, 2015: Untangling microphysical impacts on deep convection applying a novel modeling methodology. *J. Atmos. Sci.*, **72**, 2446–2464, https://doi.org/10.1175/JAS-D-14-0307.1.

——, 2019: Separating physical impacts from natural variability using piggybacking technique. *Adv. Geosci.*, **49**, 105–111, https://doi.org/10.5194/adgeo-49-105-2019.

——, 2020: Comparison of Eulerian bin and Lagrangian particle-based schemes in simulations of Pi Chamber dynamics and microphysics. *J. Atmos. Sci.*, **77**, 1151–1165, https://doi.org/10.1175/JAS-D-19-0216.1.

——, and T. L. Clark, 1991: Cloud–environment interface instability: Rising thermal calculations in two spatial dimensions. *J. Atmos. Sci.*, **48**, 527–546, https://doi.org/10.1175/1520-0469(1991)048<0527:CIIRTC>2.0.CO;2.

——, and ——, 1993: Cloud–environment interface instability: Part II: Extension to three spatial dimensions. *J. Atmos. Sci.*, **50**, 555–573, https://doi.org/10.1175/1520-0469(1993)050<0555:CEIIPI>2.0.CO;2.

——, and P. K. Smolarkiewicz, 2002: A multiscale anelastic model for meteorological research. *Mon. Wea. Rev.*, **130**, 939–956, https://doi.org/10.1175/1520-0493(2002)130<0939:AMAMFM>2.0.CO;2.

——, and L.-P. Wang, 2013: Growth of cloud droplets in a turbulent environment. *Annu. Rev. Fluid Mech.*, **45**, 293–324, https://doi.org/10.1146/annurev-fluid-011212-140750.

——, and D. Jarecka, 2015: Modeling condensation in shallow nonprecipitating convection. *J. Atmos. Sci.*, **72**, 4661–4679, https://doi.org/10.1175/JAS-D-15-0091.1.

——, and H. Morrison, 2016: Untangling microphysical impacts on deep convection applying a novel modeling methodology. Part II: Double-moment microphysics. *J. Atmos. Sci.*, **73**, 3749–3770, https://doi.org/10.1175/JAS-D-15-0367.1.

——, and G. C. Abade, 2017: Broadening of cloud droplet spectra through eddy hopping: Turbulent adiabatic parcel simulations. *J. Atmos. Sci.*, **74**, 1485–1493, https://doi.org/10.1175/JAS-D-17-0043.1.

——, and H. Morrison, 2017: Modeling condensation in deep convection. *J. Atmos. Sci.*, **74**, 2247–2267, https://doi.org/10.1175/JAS-D-16-0255.1.

——, M. Andrejczuk, and L.-P. Wang, 2011: Droplet growth in a bin warm-rain scheme with Twomey CCN activation. *Atmos. Res.*, **99**, 290–301, https://doi.org/10.1016/j.atmosres.2010.10.020.

——, P. Dziekan, and H. Pawlowska, 2018: Lagrangian condensation microphysics with Twomey CCN activation. *Geosci. Model Dev.*, **11**, 103–120, https://doi.org/10.5194/gmd-11-103-2018.

——, H. Morrison, S. Shima, G. C. Abade, P. Dziekan, and H. Pawlowska, 2019: Modeling of cloud microphysics: Can we do better? *Bull. Amer. Meteor. Soc.*, **100**, 655–672, https://doi.org/10.1175/BAMS-D-18-0005.1.

Grinstein, F. F., L. G. Margolin, and W. J. Rider, 2007: *Implicit Large Eddy Simulation: Computing Turbulent Fluid Dynamics*. Cambridge University Press, 578 pp.

Hoffmann, F., S. Raasch, and Y. Noh, 2015: Entrainment of aerosols and their activation in a shallow cumulus cloud studied with a coupled LCM–LES approach. *Atmos. Res.*, **156**, 43–57, https://doi.org/10.1016/j.atmosres.2014.12.008.

——, T. Yamaguchi, and G. Feingold, 2019: Inhomogeneous mixing in Lagrangian cloud models: Effects on the production of precipitation embryos. *J. Atmos. Sci.*, **76**, 113–133, https://doi.org/10.1175/JAS-D-18-0087.1.

Jensen, J. B., P. H. Austin, M. B. Baker, and A. M. Blyth, 1985: Turbulent mixing, spectral evolution and dynamics in a warm cumulus cloud. *J. Atmos. Sci.*, **42**, 173–192, https://doi.org/10.1175/1520-0469(1985)042<0173:TMSEAD>2.0.CO;2.

Khain, A. P., and Coauthors, 2015: Representation of microphysical processes in cloud-resolving models: Spectral (bin) microphysics versus bulk parameterization. *Rev. Geophys.*, **53**, 247–322, https://doi.org/10.1002/2014RG000468.

Kogan, Y. L., 1991: The simulation of a convective cloud in a 3-D model with explicit microphysics. Part I: Model description and sensitivity experiments. *J. Atmos. Sci.*, **48**, 1160–1189, https://doi.org/10.1175/1520-0469(1991)048<1160:TSOACC>2.0.CO;2.

Krueger, S. K., C.-W. Su, and P. A. McMurtry, 1997: Modeling entrainment and finescale mixing in cumulus clouds. *J. Atmos. Sci.*, **54**, 2697–2712, https://doi.org/10.1175/1520-0469(1997)054<2697:MEAFMI>2.0.CO;2.

Lasher-Trapp, S. G., W. A. Cooper, and A. M. Blyth, 2005: Broadening of droplet size distributions from entrainment and mixing in a cumulus cloud. *Quart. J. Roy. Meteor. Soc.*, **131**, 195–220, https://doi.org/10.1256/qj.03.199.

Margolin, L. G., and W. J. Rider, 2002: A rationale for implicit turbulence modelling. *Int. J. Numer. Methods Fluids*, **39**, 821–841, https://doi.org/10.1002/fld.331.

——, ——, and F. F. Grinstein, 2006: Modeling turbulent flow with implicit LES. *J. Turbul.*, **7**, 1–27, https://doi.org/10.1080/14685240500331595.

Matheou, G., D. Chung, L. Nuijens, B. Stevens, and J. Teixeira, 2011: On the fidelity of large-eddy simulation of shallow precipitating cumulus convection. *Mon. Wea. Rev.*, **139**, 2918–2939, https://doi.org/10.1175/2011MWR3599.1.

Morrison, H., and W. W. Grabowski, 2008: Modeling supersaturation and subgrid-scale mixing with two-moment bulk warm microphysics. *J. Atmos. Sci.*, **65**, 792–812, https://doi.org/10.1175/2007JAS2374.1.

——, M. Witte, G. H. Bryan, J. Y. Harrington, and Z. J. Lebo, 2018: Broadening of modeled cloud droplet spectra using bin microphysics in an Eulerian spatial domain. *J. Atmos. Sci.*, **75**, 4005–4030, https://doi.org/10.1175/JAS-D-18-0055.1.

Moser, D. H., and S. Lasher-Trapp, 2017: The influence of successive thermals on entrainment and dilution in a simulated cumulus congestus. *J. Atmos. Sci.*, **74**, 375–392, https://doi.org/10.1175/JAS-D-16-0144.1.

Ovtchinnikov, M., and R. C. Easter, 2009: Nonlinear advection algorithms applied to interrelated tracers: Errors and implications for modeling aerosol–cloud interactions. *Mon. Wea. Rev.*, **137**, 632–644, https://doi.org/10.1175/2008MWR2626.1.

Prabha, T. V., and Coauthors, 2012: Spectral width of premonsoon and monsoon clouds over Indo-Gangetic valley. *J. Geophys. Res.*, **117**, D20205, https://doi.org/10.1029/2011JD016837.

Pruppacher, H. R., and J. D. Klett, 1997: *Microphysics of Clouds and Precipitation*. Kluwer, 954 pp.

Riechelmann, T., Y. Noh, and S. Raasch, 2012: A new method for large-eddy simulations of clouds with Lagrangian droplets including the effects of turbulent collision. *New J. Phys.*, **14**, 065008, https://doi.org/10.1088/1367-2630/14/6/065008.

Sato, Y., S. Shima, and H. Tomita, 2018: Numerical convergence of shallow convection cloud field simulations: Comparison between double-moment Eulerian and particle-based Lagrangian microphysics coupled to the same dynamical core. *J. Adv. Model. Earth Syst.*, **10**, 1495–1512, https://doi.org/10.1029/2018MS001285.

Shima, S.-I., K. Kusano, A. Kawano, T. Sugiyama, and S. Kawahara, 2009: The superdroplet method for the numerical simulation of clouds and precipitation: A particle-based and probabilistic microphysics model coupled with a non-hydrostatic model. *Quart. J. Roy. Meteor. Soc.*, **135**, 1307–1320, https://doi.org/10.1002/qj.441.

Siebesma, A. P., and Coauthors, 2003: A large eddy simulation intercomparison study of shallow cumulus convection. *J. Atmos. Sci.*, **60**, 1201–1219, https://doi.org/10.1175/1520-0469(2003)60<1201:ALESIS>2.0.CO;2.

Smolarkiewicz, P. K., 1984: A fully multidimensional positive definite advection transport algorithm with small implicit diffusion. *J. Comput. Phys.*, **54**, 325–362, https://doi.org/10.1016/0021-9991(84)90121-9.

——, and T. L. Clark, 1986: The multidimensional positive definite advection transport algorithm. Further development and applications. *J. Comput. Phys.*, **67**, 396–438, https://doi.org/10.1016/0021-9991(86)90270-6.

——, and W. W. Grabowski, 1990: The multidimensional positive definite advection transport algorithm: Nonoscillatory option. *J. Comput. Phys.*, **86**, 355–375, https://doi.org/10.1016/0021-9991(90)90105-A.

Sölch, I., and B. Kärcher, 2010: A large-eddy model for cirrus clouds with explicit aerosol and ice microphysics and Lagrangian ice particle tracking. *Quart. J. Roy. Meteor. Soc.*, **136**, 2074–2093, https://doi.org/10.1002/qj.689.

Stevens, D. E., A. S. Ackerman, and C. S. Bretherton, 2002: Effects of domain size and numerical resolution on the simulation of shallow cumulus convection. *J. Atmos. Sci.*, **59**, 3285–3301, https://doi.org/10.1175/1520-0469(2002)059<3285:EODSAN>2.0.CO;2.

Su, C.-W., S. K. Krueger, P. A. McMurtry, and P. H. Austin, 1998: Linear eddy modeling of droplet spectral evolution during entrainment and mixing in cumulus clouds. *Atmos. Res.*, **47–48**, 41–58, https://doi.org/10.1016/S0169-8095(98)00039-8.

Thomas, S., M. Ovchinnikov, F. Yang, D. van der Voort, W. Cantrell, S. K. Krueger, and R. A. Shaw, 2019: Scaling of an atmospheric model to simulate turbulence and cloud microphysics in the Pi Chamber. *J. Adv. Model. Earth Syst.*, **11**, 1981–1994, https://doi.org/10.1029/2019MS001670.

Twomey, S., 1959: The nuclei of natural cloud formation part II: The supersaturation in natural clouds and the variation of cloud droplet concentration. *Pure Appl. Geophys.*, **43**, 243–249, https://doi.org/10.1007/BF01993560.

Warner, J., 1955: The water content of cumuliform cloud. *Tellus*, **7**, 449–457, https://doi.org/10.3402/tellusa.v7i4.8917.

——, 1969: The microstructure of cumulus cloud. Part I. General features of the droplet spectrum. *J. Atmos. Sci.*, **26**, 1049–1059, https://doi.org/10.1175/1520-0469(1969)026<1049:TMOCCP>2.0.CO;2.

Weil, J. C., P. P. Sullivan, and C. Moeng, 2004: The use of large-eddy simulations in Lagrangian particle dispersion models. *J. Atmos. Sci.*, **61**, 2877–2887, https://doi.org/10.1175/JAS-3302.1.